J. Fluid Mech. (1995), *vol.* 283, *pp.* 141–173

Impact of drops on solid surfaces: self-similar capillary waves, and splashing as a new type of kinematic discontinuity

By A. L. YARIN[1] AND D. A. WEISS[2,3]†

[1] Faculty of Mechanical Engineering, Technion – Israel Institute of Technology, Haifa 32000, Israel

[2] Max-Planck-Institut für Strömungsforschung, Bunsenstraße 10, 37073 Göttingen, Germany

[3] Laboratoire d'Aérothermique du CNRS, 4ter Route des Gardes, 92190 Meudon, France

(Received 9 December 1993 and in revised form 17 August 1994)

The impact of drops impinging one by one on a solid surface is studied experimentally and theoretically. The impact process is observed by means of a charge-coupled-device camera, its pictures processed by computer. Low-velocity impact results in spreading and in propagation of capillary waves, whereas at higher velocities splashing (i.e. the emergence of a cloud of small secondary droplets, absent in the former case) sets in. Capillary waves are studied in some detail in separate experiments. The dynamics of the extension of liquid lamellae produced by an impact in the case of splashing is recorded. The secondary-droplet size distributions and the total volume of these droplets are measured, and the splashing threshold is found as a function of the impact parameters.

The pattern of the capillary waves is predicted to be self-similar. The calculated wave profile agrees well with the experimental data. It is shown theoretically that the splashing threshold corresponds to the onset of a velocity discontinuity propagating over the liquid layer on the wall. This discontinuity shows several aspects of a shock. In an incompressible liquid such a discontinuity can only exist in the presence of a sink at its front. The latter results in the emergence of a circular crown-like sheet virtually normal to the wall and propagating with the discontinuity. It is predicted theoretically and recorded in the experiment. The crown is unstable owing to the formation of cusps at the free rim at its top edge, which results in the splashing effect. The onset velocity of splashing and the rate of propagation of the kinematic discontinuity are calculated and the theoretical results agree fairly well with the experimental data. The structure of the discontinuity is shown to match the outer solution.

1. Introduction

Drop impact on solid surfaces is a phenomenon encountered in a wide variety of fields, e.g. ink jet printing, soil erosion by rain, spray cooling, annealing, quenching and painting, shock atomizing, engines, meteorology. In spite of its commonness, and although some of its features have been known for decades (see e.g. Worthington, 1876, 1877, 1908), the mechanism of drop impact, especially in the case of multiple drops, is far from clear. Reviews of the present state of knowledge can be found in Prosperetti & Oğuz (1993) and Rein (1993) and references therein; some of them, as well as additional ones, are discussed below.

† Present address: Faculty of Mechanical Engineering, Technion – Israel Institute of Technology, Haifa 32000, Israel.

Several cases are generally to be considered as essentially distinct. Drops can hit a solid or a wet surface, which in the latter case can be that of a deep or shallow liquid. Sometimes bouncing of a drop takes place; in the case of heated solid surface the Leidenfrost effect may be responsible (Rein 1993; Fukai *et al.* 1993; Naber & Farrell 1993; Labeish 1994). The impact of a solitary drop differs from that of a train of drops (impinging one by one), as is the case in most situations of practical interest. The non-triviality of such situations has been recognized by Riedel (1977) mainly in acoustic effects.

In the present paper we investigate in detail the impact of drop trains onto a solid surface which is initially dry but acquires a liquid film in the steady state at the moments of impact. Our main goals are a physical model for the self-similar capillary waves, as well as the splashing phenomenon, and estimation of the splashing threshold.

In the experimental part of the work it is shown that there is a universal dependence of the critical impact velocity, V_{0s}, at which splashing first occurs, on the physical parameters of the liquid (i.e. its density, surface tension and kinematic viscosity) and on the frequency of the drop train. For impact velocities $V_0 < V_{0s}$ a drop spreads over the wall in the form of a thin liquid film without any secondary droplet formation, with the impact energy totally absorbed, first, by capillary waves. (These waves are studied in a separate experiment.) On the other hand, for $V_0 > V_{0s}$ experimental results of the present work, as well as those of Levin & Hobbs (1971), show a completely distinct picture. Upon impact on shallow liquid layer (in our case the film produced by preceding drops), a crown-like liquid sheet, virtually normal to the film, emerges and propagates radially from the centre of impact. At its top edge, owing to the action of surface tension, there immediately appears a free rim propagating over it towards the wall (see e.g. figure 8 in Levin & Hobbs 1971 and the photograph of Edgerton & Killian in Allen 1988 and Peregrine, Shoker & Symon 1990, as well as the detailed studies of the free rims at the edges of free liquid films in Taylor 1959 and Yarin 1993). Taylor (1959) showed that the free rims propagate with a velocity independent of their local curvature. Therefore being (inevitably) disturbed the free rims produce cusps, which is readily seen by applying the Huygens principle (Yarin 1993, pp. 27–28). Cusp formation is considered in more detail below in §8. At the cusp sites thin liquid jets are formed, which are unstable – again owing to the action of surface tension (capillary instability of the Rayleigh type) – with eventual breakup and formation of very small droplets (see the sketch in figure 1 as well as figure 8 in Levin & Hobbs 1971, where the cusps and thin liquid jets outflowing from them are clearly seen; see also figure 16 below).

It should be emphasized that in the splashing phenomenon the role of gravity is negligible owing to the small scales involved, and only inertia and surface tension are of importance. By contrast, in the hydraulic jump phenomenon gravity is the driving force even where surface tension has to be taken into account (Liu & Lienhard 1993). Thus splashing and hydraulic jumps are totally distinct phenomena.

Theoretical models of various stages of splashing have been proposed by several authors. Engel (1955), Bowden & Field (1964), Lesser (1981) and Lesser & Field (1983) worked out the modelling of the compressibility effect, which is of importance at the early stage of splashing, leading to jetting of a drop over a solid surface. Below in §§3 and 8 we use the results of Bowden & Field (1964) to estimate the effect of compressibility in the present case (it is shown that this effect is negligibly small under the conditions of our experiment).

Allen (1975) tried to explain the small fingering seen sometimes at the circumference of a drop impacting a solid surface (see also Engel 1955 and Loehr & Lasek 1990). He

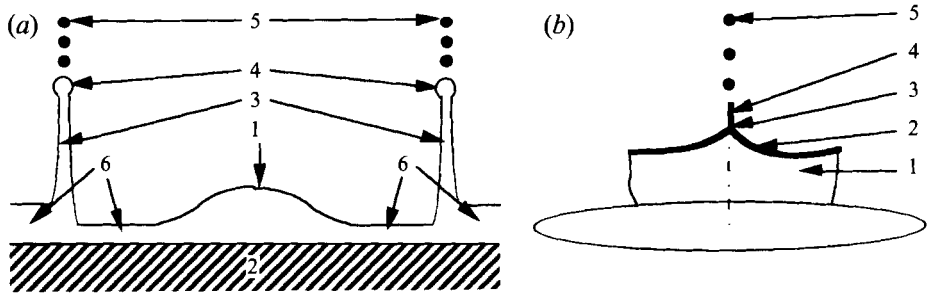

FIGURE 1. (*a*) Sketch of splashing mechanism: 1, residual top of impacting drop; 2, wall; 3, section of crown-like sheet propagating outwards; 4, cross-section of free rim; 5, secondary droplets formed from cusps of free rim; 6, liquid layer on wall. (*b*) Free rim and secondary droplets magnified: 1, crown-like sheet; 2, free rim at its top edge; 3, cusp; 4, thin jet emerging at cusp; 5, secondary droplets formed on breakup of jet.

considers the circumferencial section of the interface moving radially outwards and decelerating by friction forces from the solid surface. He argues that it should be subject to Rayleigh–Taylor instability. However, to match the experimental evidence with such a model requires a deceleration of the order or $-160\,g$ (g is the gravity acceleration), which seems to be too high.

Peregrine (1981) proposed a model which might be used to predict crown propagation in splashing. The model supposes the flow to be steady in the neighbourhood of the impact point and crown basement (in the reference frame 'frozen' there). It is based essentially on the steady Bernoulli equation. Therefore it predicts a constant (time-independent) speed of crown propagation. The data of Levin & Hobbs (1971), as well as the experimental results of the present work, show that this is not the case in the splashing of drops. Thus the model of Peregrine (1981) cannot be applied to this essentially non-steady phenomenon. Nevertheless, this model might be helpful in large-scale splashes which is the main focus in Peregrine (1981).

In §2 the experimental set-up used, consisting of the equipment and the algorithms developed for picture evaluation, is described. In §3 the results of the experiments are reported.

At first sight the real pattern of splashing appears too complicated for any theoretical treatment except a numerical one (see e.g. Harlow & Shannon 1967; Prosperetti & Oğuz 1993). However, in §§4–7 we show that the underlying mechanism and its description may be readily represented by a relatively simple quasi-one-dimensional model. In §4 we obtain the governing equations of the surface-tension-dominated flow in a thin liquid film on a wall. In §5 we discuss briefly the propagation of capillary waves over such a film and find self-similar regimes. The splashing condition is derived in §6. The physical nature of splashing is explained in terms of a kinematic discontinuity formation, with a sink at its front, apparently of a new type – a discontinuity (a kind of shock wave) in an *incompressible liquid*. In §7 we address the structure of this discontinuity. The theoretical results are compared in §8 with the experimental data of §3 where the discussion is presented. The conclusions are summarized in §9.

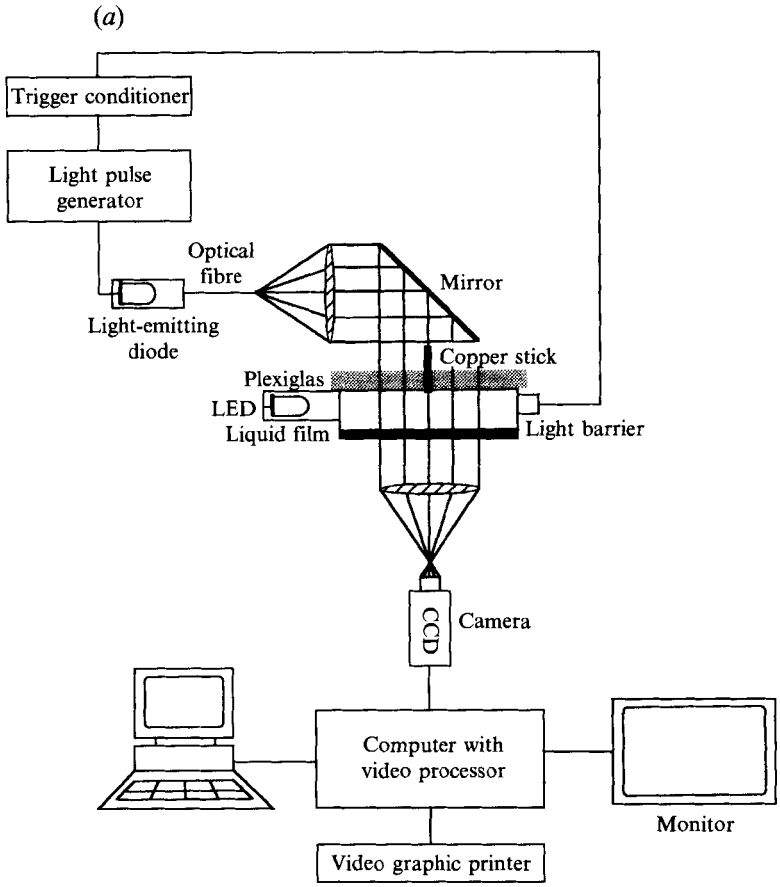

FIGURE 2(*a*). For caption see facing page.

2. Experimental set-up

2.1. *Equipment*

Capillary waves are excited here by the impact of a thin stick (thickness 0.4 mm) of copper onto a liquid film of ethanol (thickness 1.4 mm). The stick falls along its axis perpendicularly to the film surface. The wave patterns are observed by means of a charge-coupled-device camera from below the film. They are illuminated from above by flashes of a light-emitting diode (LED) fed by a light-pulse generator, which in turn is triggered by a light barrier. The delay of the flash can be varied continuously from 1 μs to 1 s. The camera takes pictures with 25 Hz and forwards them to a computer, where they can be supervised on a monitor and eventually be printed out by a video graphic printer.

The experimental set-up to observe capillary waves is shown schematically in figure 2(*a*). The observation technique is essentially a shadowgraph technique, dark and bright areas in the pictures correspond to sites with positive and negative curvature of the free film surface, respectively.

Monodisperse drops are produced by a technique developed by Schneider & Hendricks (1964) and further by Lindblad & Schneider (1965). A free jet is modulated by an oscillating piezoelectric crystal, situated upstream of the nozzle, and breaks up according to Rayleigh instability into drops of equal size which can be varied within

(*b*)

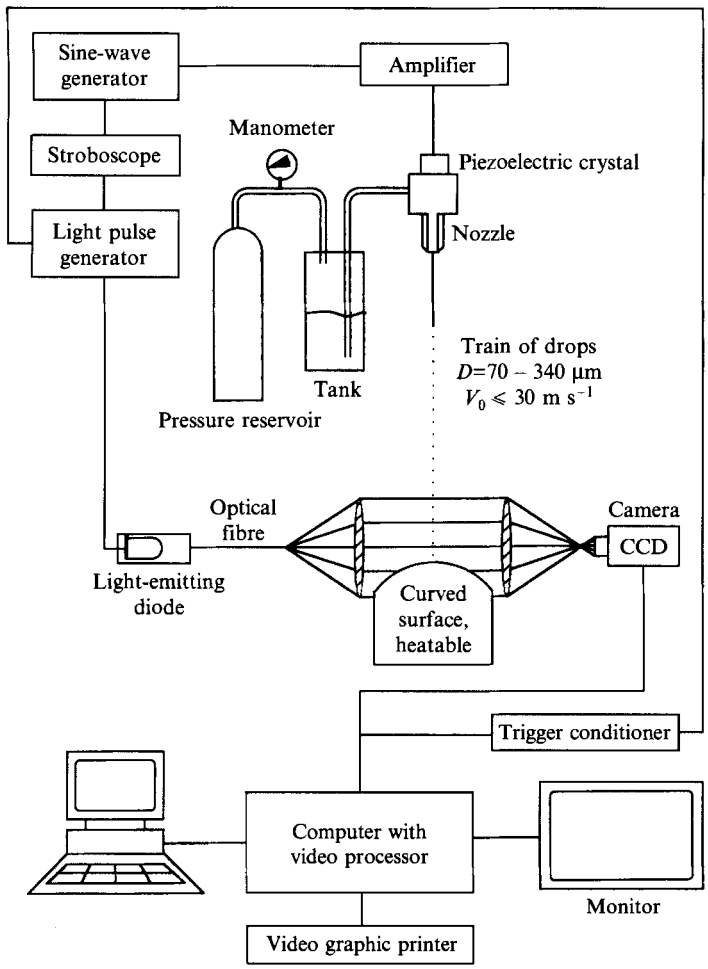

FIGURE 2. Experimental set-up: (*a*) investigation of capillary waves, (*b*) investigation of drop impact.

a certain range for a fixed jet velocity. Different nozzle diameters are used here, and the drop diameter can be chosen from about 70 to 340 μm. The jet velocity is controlled by the pressure in a reservoir, limited in our case to about 5.5 bar, allowing jet velocities up to approximately 30 m s^{-1}.

The temperature of the test liquids (essentially room level) is determined by a thermocouple element measuring the nozzle temperature.

After a distance along which the drop oscillations fade away, the drops hit a solid surface. The specimens used have mean roughnesses of $R_z \approx 1$ or 16 μm, respectively. They can be heated from below by the tips of soldering irons; their temperature is measured by an additional thermocouple element. In the experiments performed the wall temperature is kept below the boiling point of the test liquids.

The impact process is observed by means of a charge-coupled-device camera. As before, it forwards the pictures to the computer where they are processed and evaluated; they can likewise be supervised on monitor and eventually printed out by the video printer.

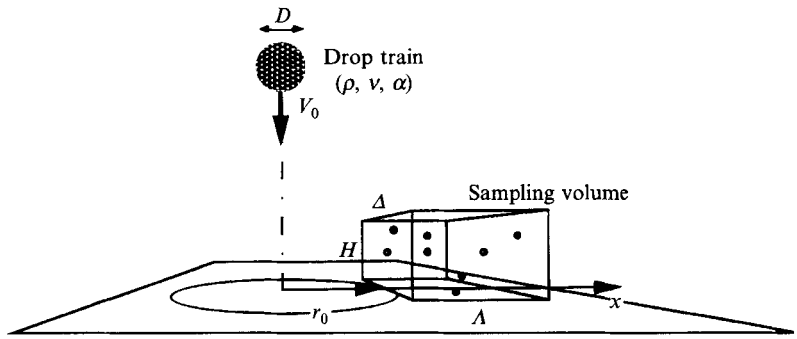

FIGURE 3. Sampling volume. H, Δ, and Λ are its height, thickness, and length, respectively. Droplet size statistics are extrapolated from this sampling volume to the impact process; the method works only if $\Delta \lesssim r_0$, the radial distance of the front wall of the sampling volume from the impact site. The x-axis is perpendicular to the front wall of the sampling volume and lies within the focal plane of the camera. Here $r_0 \approx 1$ mm, $H \approx 2$ mm, $\Delta \approx 0.85$ mm, $\Lambda \approx 3$ mm.

The modified experimental set-up to observe drop impact is shown schematically in figure 2(*b*). The site of drop impact on the solid surface is illuminated by the light of a LED triggered by the signal generator, i.e. the same source as the piezoelectric crystal, and fed by a light-pulse generator which in turn is actuated by a stroboscope, whereby the phase of its flash can be shifted between 0 and 2π. There is also provision for illuminating by single flashes, in which case the light-pulse generator waits for the conditioned ready signal of the camera.

Drop velocity is determined as the product of the signal generator's frequency and the spacing of the successive drops, which, in turn, is measured from the pictures.

All test liquids are Newtonian. Their density, surface tension, viscosity, and in one case also velocity of sound, are varied over a fairly wide range. Most experiments are performed with ethanol or mixtures of ethanol, glycerol, and water. The density is determined by measuring the mass of a known volume of the liquid. The surface tension is measured statically with a tensiometer, and the viscosity is determined with capillary viscometers. The velocity of sound is taken from the literature.

2.2. *Computer-aided picture evaluation*

As described in the preceding subsection, the impact process is recorded by means of a CCD camera. Evaluation of the pictures was intended to be performed by computer as far as possible. New algorithms were developed for that purpose (Weiss 1993), permitting determination of the diameter and velocity of the incoming drops (if two or more drops are shown on the same picture), as well as the number and sizes of the secondary droplets formed if the drops splash (cf. §3), and thereby the total mass fraction ejected in the form of droplets.

The basic task of the algorithms is to recognize sharply represented (well-focused) drops or droplets, using a technique presented by Fantini, Tognotti & Tonazzini (1990), whereby drops are essentially recognized as well-focused if the grey area between their dark core and the bright background, i.e. their 'halo', is narrow enough. Sizes and centre-of-mass coordinates are determined by means of contour integrals, so that bright spots within dark drops have no effect. To obtain true sizes instead of a number of picture elements, the algorithm has to be calibrated by taking photographs of transparent rulers.

With these basic routines it is possible to determine the drop impact velocity and secondary droplet size distributions. For the former, the average spacing of successive

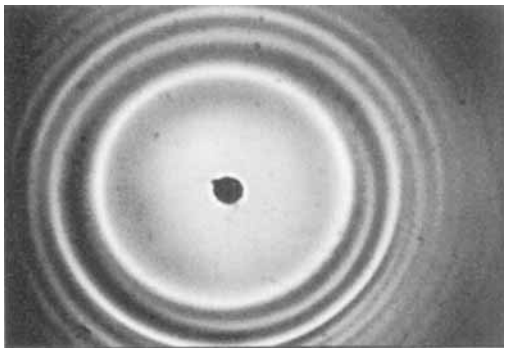

FIGURE 4. Pattern of capillary waves taken 5 ms after impact of a copper stick onto an ethanol film of 1.4 mm thickness. The whole picture covers an area of about 25 mm × 35 mm.

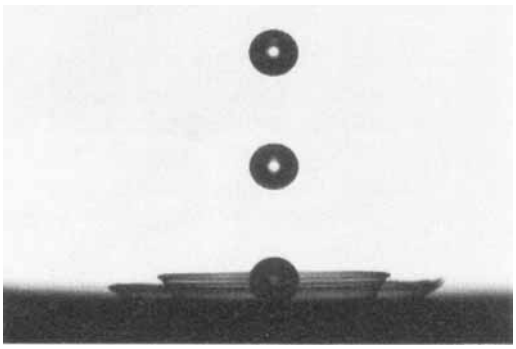

FIGURE 5. Spreading ethanol drops stroboscopically illuminated; spreading lamellae at two different stages can be recognized. Drop diameter $D = 279$ μm, impact velocity $V_0 = 7.8$ m s^{-1}, $u = 16.9$.

drops is multiplied by the impact frequency, whereas for the latter the statistics extracted from a picture series of a sampling volume (figure 3) are extrapolated to the full impact process. A series consists of 20 pictures, so the statistical results obtained are reliable. The thickness Δ of the sampling volume was determined by calibration measurements. The extrapolation takes into account that the droplets have to be weighted by an x-dependent factor before the sum over x is calculated. In the experimental set-up the x-axis is parallel to the solid surface and perpendicular to the direction of observation, i.e. parallel to the focal plane of the camera.

3. Capillary waves, spreading and splashing drops

3.1. *Surface elevations*

Capillary waves are observed using the technique described in §2. An example is shown in figure 4. Dark and bright concentric rings can be recognized. It is seen that the stick is thin enough for our purposes. For evaluation the radii of the dark rings are measured, which have to be compared with the maxima of the curvature of the calculated film profile (cf. §§5 and 8).

3.2. *The splashing threshold*

In the investigated range of impact velocities the drops initially take the shape of lamellae because they spread along the wall from which their rims seem to issue. A stroboscopically illuminated picture of such lamellae is shown in figure 5, where two different stages can be recognized.

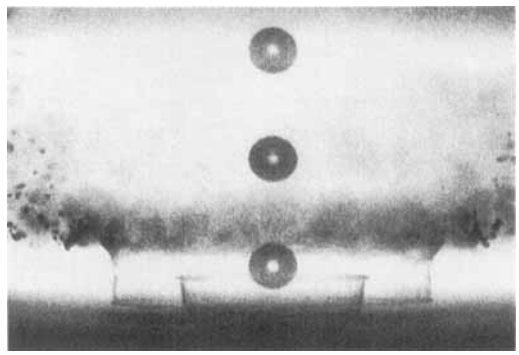

FIGURE 6. Splashing ethanol drops illuminated by single flash. Drop diameter $D = 276$ μm, impact velocity $V_0 = 12.7$ m s^{-1}, $u = 22.5$.

With the impact parameters, i.e. velocity, frequency, and drop diameter, suitably chosen the lamellae later take the shape of crowns; their lower part consists of a thin liquid sheet and at the upper part the sheets are unstable forming the rims of the crowns, from which small secondary droplets are ejected. The drops begin to splash. Figure 6 shows a picture of splashing drops illuminated by a single flash. Note that the term 'droplets' (or secondary droplets) refers to what is ejected from the rim of the crowns, whereas 'drops' are what hits the solid wall.

In order to obtain a quantitative condition for the drops to splash, the splashing threshold is determined for different values of drop diameter D, frequency f, and velocity V_0 as well as of the mean wall roughness R_z, its temperature and also of the liquid density, surface tension, viscosity, and even the velocity of sound.

The procedure is as follows. For a chosen test liquid, the frequency f to splash is determined as a function of the pressure in the reservoir (i.e. the drop velocity). It is observed that reducing the frequency for a fixed velocity promotes splashing; thus one might conclude from continuity arguments that larger drops generally begin to splash at lower velocities than smaller ones. This conjecture, however, is disproved by the data plotted in figure 7. It is evident that for a chosen liquid the drop velocity and its diameter alone do not describe the impact process completely. The drop velocity at the splashing threshold is not even a single-valued function of the drop diameter, but also depends on another parameter, e.g. the nozzle diameter ϕ. Another consequence is that the splashing threshold cannot be described by a single-drop Reynolds number $Re = V_0 D/\nu$ or Weber number $We = \rho D V_0^2/\alpha$ (V_0 being the impact velocity, D the drop diameter, and ρ, α, and ν are the density, surface tension and kinematic viscosity, respectively). Nevertheless, the splashing threshold can be characterized by a single dimensionless number, because the capillary number $Ca = \rho V_0 \nu/\alpha = We/Re$ is a simple function of a non-dimensional 'viscosity length' $\lambda = (\nu/f)^{1/2}\alpha/(\rho\nu^2)$ at the splashing threshold. This function is plotted in figure 8 for the two surface specimens used. It describes the splashing threshold by the correlation $Ca = C\lambda^{-3/4}$, where the coefficient C depends only slightly on the mean surface roughness R_z (at least as long as $R_z \ll D$), and which can be rewritten as $Ca\,\lambda^{3/4} = V_0(\rho/\alpha)^{1/4}\nu^{-1/8}f^{-3/8} = u = C \approx 17$ to 18, where the dimensionless impact velocity u is introduced. For figure 8 the parameters $Ca = \rho V_0 \nu/\alpha$ and $\lambda = (\nu/f)^{1/2}\alpha/(\rho\nu^2)$ were typically known to an accuracy of about 2 to 4%: V_0, ν, α, ρ and f were known up to about 0.3 to 0.5, 2, 0.5, 0.3 and 0.1 %, respectively.

The splashing threshold at $u = 17$ to 18 corresponds to developed crown instability,

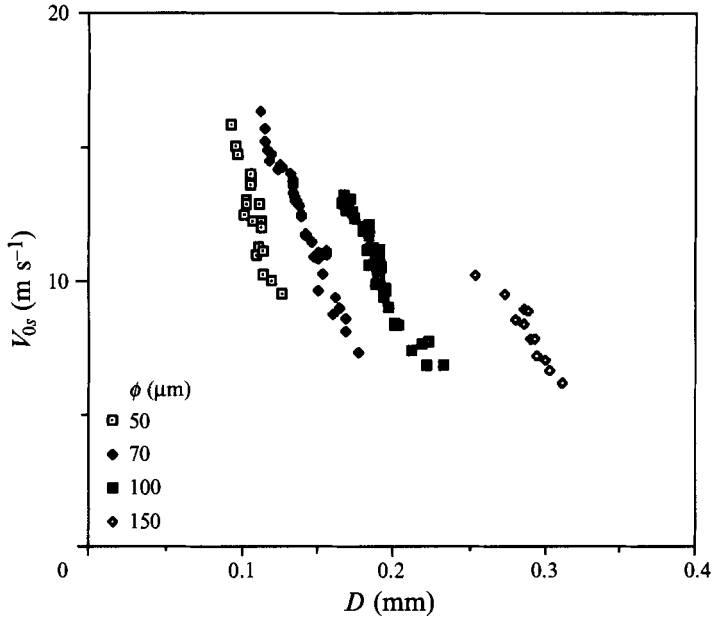

FIGURE 7. Impact velocity at splashing threshold V_{0s} as function of drop diameter for ethanol and surface specimen with roughness $R_z = 1$ μm at room temperature. Drop diameter and velocity do not describe the impact process completely even for a single liquid. Another quantity (e.g. nozzle diameter) must thus be of importance since V_{0s} is not a single-valued function of D. The different symbols correspond to different nozzle diameters ϕ.

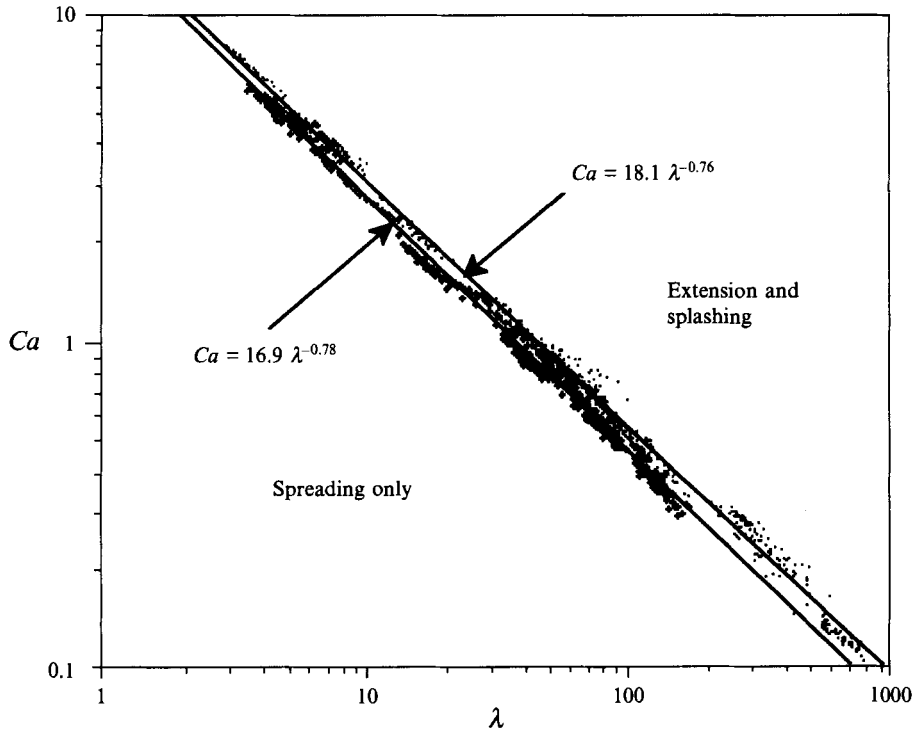

FIGURE 8. Splashing threshold. Capillarity number as function of non-dimensional 'viscosity length'. The threshold can be described by the correlation $Ca = C\lambda^{-3/4}$. ●, Surface roughness $R_z = 1$ μm; +, $R_z = 16$ μm.

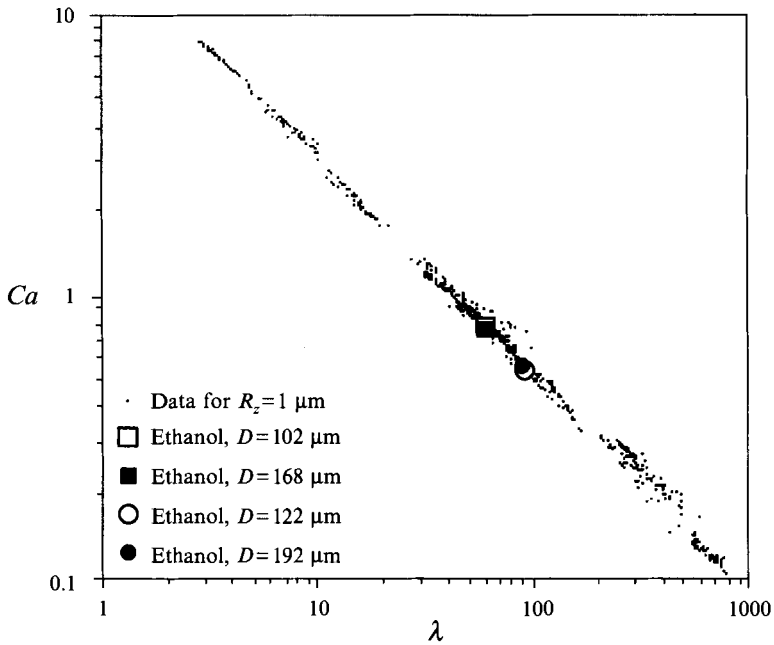

FIGURE 9. Splashing threshold: comparison of selected data points obtained for surface roughness $R_z = 1$ μm; the drop diameter does not enter the correlation at the onset of splashing.

strong enough to produce a cloud of secondary droplets. In some cases below this threshold, a crown is not high enough or the process is not long enough to produce secondary droplets (e.g. figure 5). Therefore crown formation begins slightly below the splashing threshold.

It is emphasized that it was impossible to correlate the onset of splashing with the Mach number of a liquid based on its sonic speed, which shows that under the given conditions early events related with compressibility are 'forgotten' almost instantaneously (in timescale of the whole splashing process).

It is thus not extraordinary that the drop diameter does not enter the splashing threshold correlation at all; this fact is confirmed by figure 9 and implies that the splashing process indeed has its cause in the flow within the lamella itself rather than in the drop impact details.

The fact that R_z/D hardly influences C is also easy to understand; it is clear that the drops hitting the solid surface meet a liquid film arising from the preceding drops. If this liquid film is thick compared to R_z, it is to be expected that the drops are not affected much by surface roughness. In our experiments we got an estimation for the liquid film thickness by comparing on the pictures the horizons for a dry surface and the surface while experiments were running. In this way we obtained for the film thickness h_0 values between 20 μm (for the smallest drops) and 50 μm (for the large drops). This leads to $h_0/D \approx 1/6$ typically. The film thickness h_0 can therefore be taken as large, at least as compared to $R_z = 1$ μm, and, with some care, also compared to $R_z = 16$ μm.

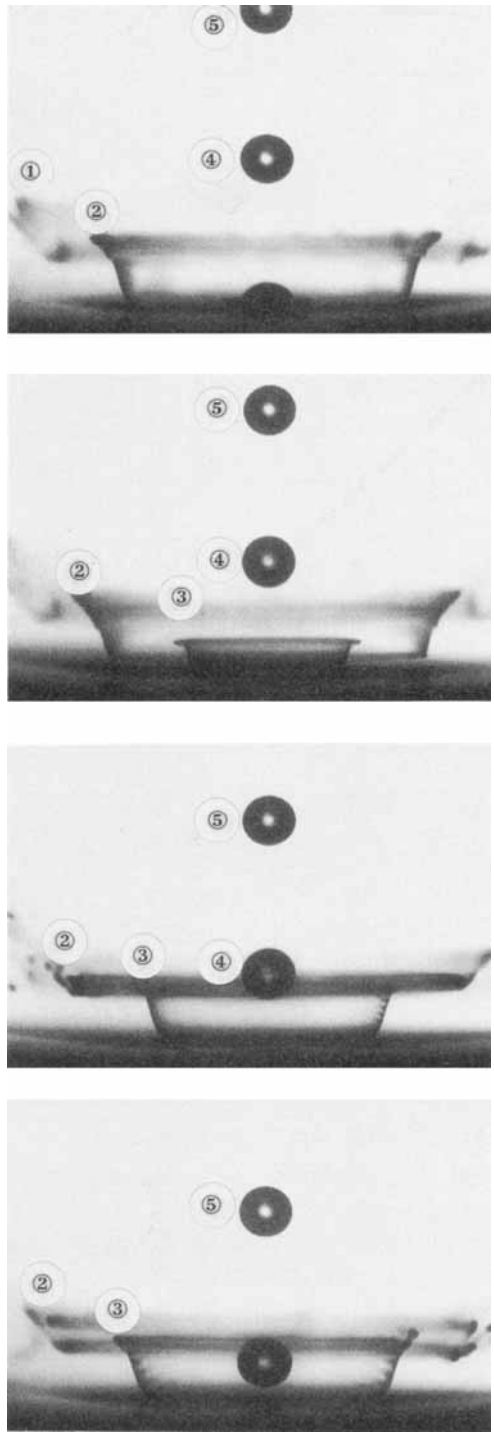

FIGURE 10. Radial extension of the splashing lamellae (ethanol drops stroboscopically illuminated). Drop diameter $D = 312$ μm, impact velocity $V_0 = 10.0$ m s^{-1}, $u = 22.3$. The phases, i.e. the non-dimensional times $\tau = 2\pi ft$ after impact, are: (*a*) $\pi/3$, (*b*) $5\pi/6$, (*c*) $4\pi/3$, and (*d*) $11\pi/6$. Note that the droplet production at the crown's rim can be more or less irregular, as can be seen in (*c*) on the left and the right side of the crown. The drops have been numbered to identify the crowns.

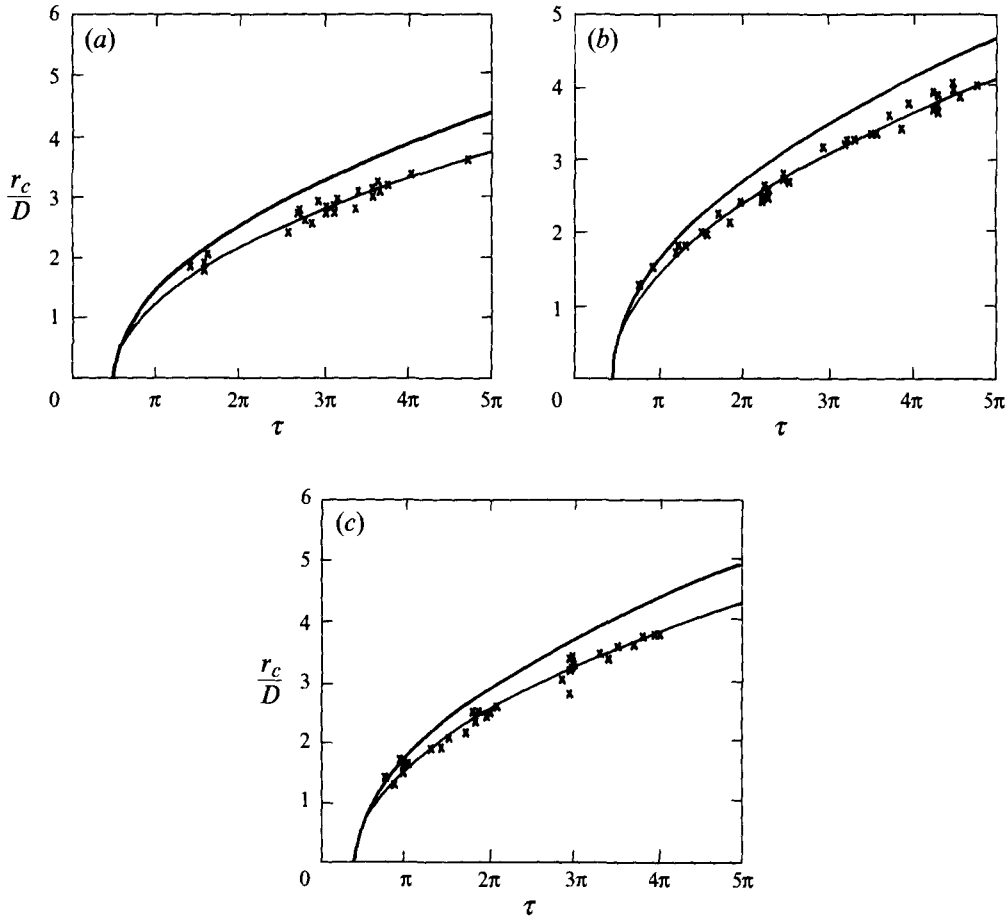

FIGURE 11. Radial position of crown's rim as function of phase, i.e. non-dimensional time $\tau = 2\pi ft$. The experimental data are indicated by the cross symbols; their best fits are shown by fine lines; the curves predicted by the theory (equation (8.7)) by bold lines. (*a*) $D = 258$ μm, $V_0 = 8.74$ m s^{-1}, $f = 16.317$ kHz, $u = 16.6$. (*b*) $D = 269$ μm, $V_0 = 11.4$ m s^{-1}, $f = 19.523$ kHz, $u = 20.2$. (*c*) $D = 271$ μm, $V_0 = 12.5$ m s^{-1}, $f = 19.973$ kHz, $u = 22.0$. The data for all these plots were obtained with ethanol drops.

3.3. *Extension kinematics of lamellae*

Having shown that the cause of splashing lies in the flow within the lamella, it is appropriate to investigate the extension of the latter. The easiest way is to measure the radial propagation of the rim of the crowns, which is illustrated by figure 10. This yielded figure 11. The distance of the rim from the impact centre (in drop diameter units) is shown as a function of the phase τ, which is time multiplied by $2\pi f$. The best-fit approximations of the experimental data given in figures 11(*a*)–11(*c*) respectively, are as follows:

$$r_c/D = 1.00(\tau - 1.54)^{1/2}, \quad r_c/D = 1.09(\tau - 1.38)^{1/2}, \quad r_c/D = 1.12(\tau - 1.28)^{1/2}, \tag{3.1a–c}$$

where r_c is the crown radius.

These best fits have been obtained by optimizing K and τ_0 in the form

$$r_c/D = K(\tau - \tau_0)^{1/2}. \tag{3.2}$$

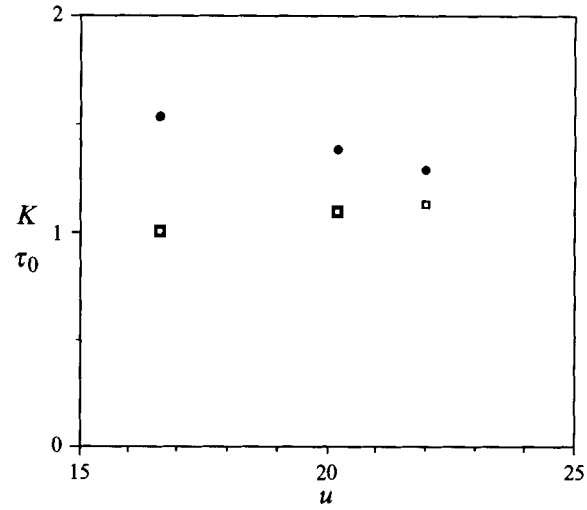

FIGURE 12. Best-fit values of K (□) and τ_0 (●) of figure 11 as functions of dimensionless impact velocity u.

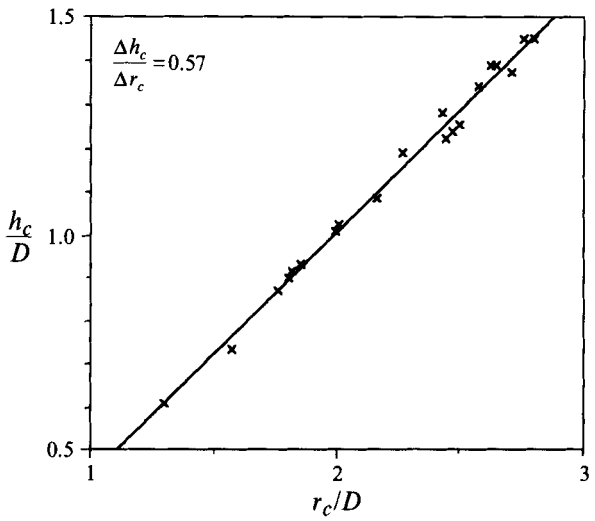

FIGURE 13. Rim elevation, corresponding to the impact of ethanol drops with $D = 269$ μm, $V_0 = 11.4$ m s^{-1}, $f = 19.523$ kHz, $u = 20.2$.

The values of K and τ_0 are plotted as functions of u in figure 12, which shows that K appears to increase, and τ_0 to decrease, with increasing u.

The elevation of the rim (measured from an arbitrarily chosen level) as a function of its radius is shown in figure 13. This function is a good approximation of a straight line. Thus gravity can be neglected up to this stage.

Instantaneous configurations of the crown generatrices below breakup points seen in figures 6 and 10 are also a good approximation of a straight line. Therefore the intact crowns are too short in this case (because crown breakup is too fast) to approximate them accurately enough by parabolic forms arising under the gravity effect, like those calculated by Peregrine (1981).

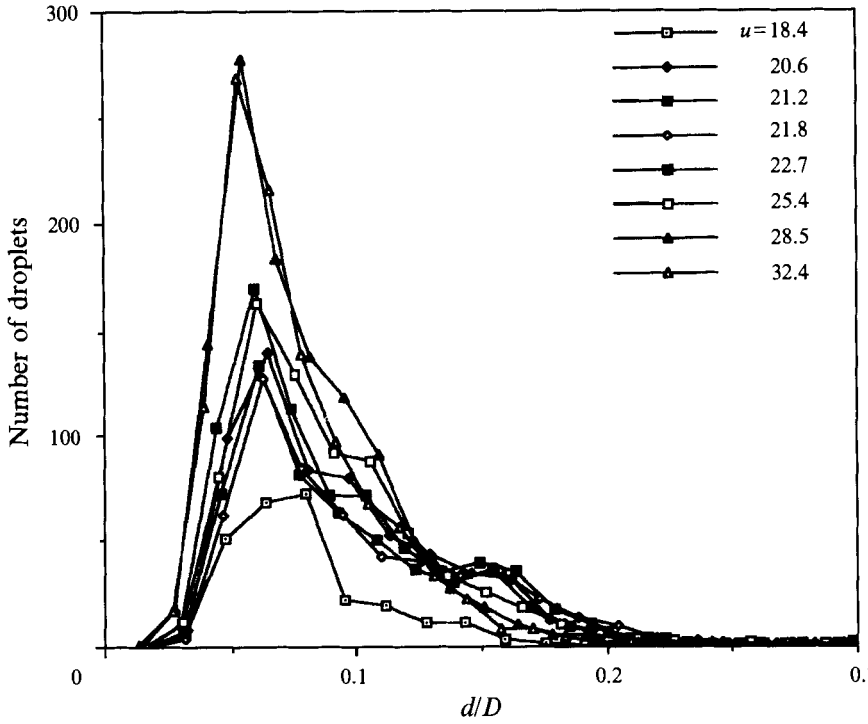

FIGURE 14. Droplet size distribution for different values of u; d is the diameter of secondary droplets.

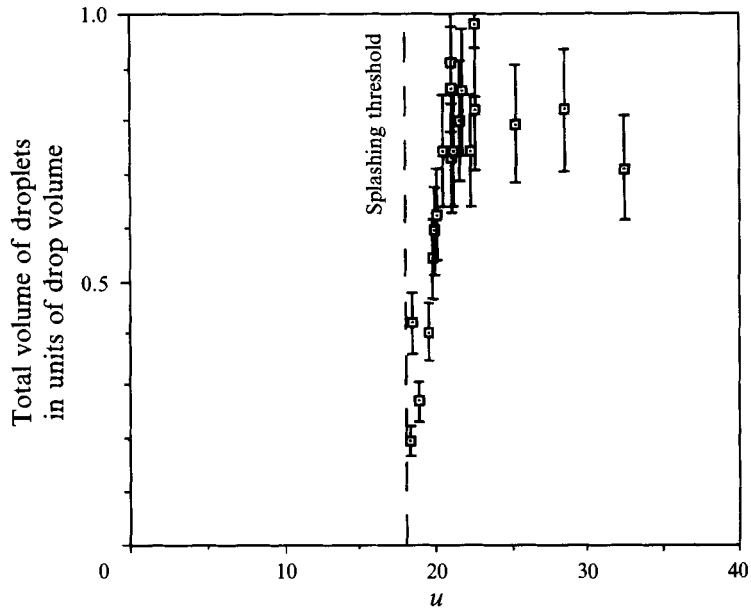

FIGURE 15. Total mass of secondary droplets in units of drop volume. The error bars denote an error of 14%, which is mainly due to the uncertainty of the thickness Δ of the sampling volume.

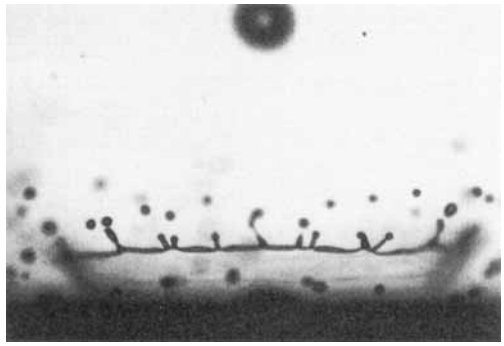

FIGURE 16. A crown's rim of a splashing lamella illuminated by a single flash.

3.4. *Droplet size distributions*

The numbers and sizes of the secondary droplets are determined by means of the technique presented in the preceding section. The experiments are performed with ethanol on the smooth-surface specimen ($R_z \approx 1$ μm). It is found that the droplet diameters cover extended spectra, ranging from nearly zero to about one-quarter of the drop diameter (cf. figure 14). The distributions have their global maximum at $d/D \approx 0.06$ and one or more bumps at larger values of d/D.

The total ejected mass is readily obtainable from the distributions in figure 14. The result is shown in figure 15. The mass fraction grows monotonically from zero at the splashing threshold, apparently tending to a limiting value which is less than 1 for larger values of u. For further details concerning the distributions, see Weiss (1993).

It may be useful to give some estimates of sizes here, i.e. a typical crown wall thickness as well as the thickness of a jet arising from a cusp. As an example we take the picture illuminated by a single flash shown in figure 16. We obtain for the crown wall thickness, δ, values of $1/50 \lesssim \delta/D \lesssim 1/15$, typically $\delta/D \approx 1/30$. For the jet thickness Δ we measure $1/15 \lesssim \Delta/D \lesssim 1/8$, typically $\Delta/D \approx 1/10$.

4. Governing equations

In this section we present a quasi-one-dimensional theory for the splashing process. It considers the flow in the liquid lamella after the impact. This approach is justified by the fact that the diameter of the impacting drops does not affect the splashing process at all, as was shown above in the experimental part.

We treat the problems of a planar and an axisymmetric geometry in parallel. For the theoretical results to be compared to the experimental ones of the present work, the axisymmetric case must be used. We consider the flow in a thin liquid film bounded on one side by a solid surface; the other surface is assumed to be free. Lengthscales are to be very small for gravity effects to be neglected. We also neglect viscosity effects for the moment (this point will be discussed below).

We adopt a simplified quasi-one-dimensional approach averaging the flow velocity over the layer thickness. Accordingly, the continuity equation for the planar case take the form

$$\frac{\partial h}{\partial t}+\frac{\partial h V}{\partial x}=0, \tag{4.1}$$

where t is time, x the coordinate along the wall, h the layer (lamella) thickness, and V the velocity. Here and hereinafter the liquid is supposed to be incompressible; as is shown below, compressibility is of importance only at the very beginning of the drop

impact process, whereas it does not affect the lamella extension nor splashing process itself.

The momentum equation expresses the balance of the inertial and surface tension forces:

$$\frac{\partial}{\partial t}(\rho h V)+\frac{\partial}{\partial x}(\rho h V^2) = -\frac{\partial}{\partial x}(p_\alpha h)+\frac{\partial}{\partial x}(F_\alpha). \tag{4.2}$$

Here ρ is density, p_α stands for the capillary pressure, and F_α is the x-projection of the surface tension force acting at the free surface:

$$p_\alpha = -\alpha\frac{\partial^2 h/\partial x^2}{[1+(\partial h/\partial x)^2]^{3/2}}, \quad F_\alpha = \frac{\alpha}{[1+(\partial h/\partial x)^2]^{1/2}} \tag{4.3a, b}$$

(α being the surface tension coefficient).

By (4.1)–(4.3) we arrive at the following form of the momentum equation:

$$\rho h\left(\frac{\partial V}{\partial t}+V\frac{\partial V}{\partial x}\right) = \alpha\frac{\partial}{\partial x}\left\{\frac{1}{[1+(\partial h/\partial x)^2]^{1/2}}+\frac{h\,\partial^2 h/\partial x^2}{[1+(\partial h/\partial x)^2]^{3/2}}\right\}. \tag{4.4}$$

In the given problem the characteristic scales of h, V, t, and x are h_0, V_0, $1/f$, and V_0/f, respectively, where h_0 is some unperturbed thickness of the layer (discussed below), V_0 the impact velocity of a drop, and f the frequency of the drop train. We assume that $(h_0 f/V_0)^2 \ll 1$, which corresponds to the experimental data (e.g. for $h_0 \lesssim 10^{-4}$ m, $f =$ 19.5 kHz, $V_0 \sim 10$ m s^{-1}, the ratio $(h_0 f/V_0)^2 \sim 10^{-2}$). Therefore we can neglect the derivative $(\partial h/\partial x)^2$ relative to unity and obtain the governing equations of the planar case in the following form:

$$\frac{\partial h}{\partial t}+\frac{\partial h V}{\partial x} = 0, \quad \rho h\left(\frac{\partial V}{\partial t}+V\frac{\partial V}{\partial x}\right) = \alpha\frac{\partial}{\partial x}\left(h\frac{\partial^2 h}{\partial x^2}\right). \tag{4.5a, b}$$

Here the unknowns are h and V.

In the axisymmetric case the continuity equation takes the form

$$\frac{\partial rh}{\partial t}+\frac{\partial rh V}{\partial r} = 0, \tag{4.6}$$

where r is the polar radius from the point of drop impact.

The momentum balance reads (with $(\partial h/\partial r)^2$ neglected relative to unity)

$$\frac{\partial}{\partial t}(\rho rh V\boldsymbol{e}_r)+\frac{\partial}{\partial r}(\rho rh V^2\boldsymbol{e}_r) = \frac{\partial}{\partial r}(-p_\alpha rh\boldsymbol{e}_r)+\frac{\partial}{\partial\phi}(-p_\alpha h\boldsymbol{e}_\phi)+\frac{\partial}{\partial r}(\alpha r\boldsymbol{e}_r)+\frac{\partial}{\partial\phi}(\alpha\boldsymbol{e}_\phi), \tag{4.7}$$

where $\boldsymbol{e}_r$ and $\boldsymbol{e}_\phi$ are the unit vectors of the radial and azimuthal directions; ϕ is the polar angle, p_α is given by (4.3a) with r instead of x.

By projecting (4.7) onto the radial direction we arrive at the following governing equations for the axisymmetric case:

$$\frac{\partial rh}{\partial t}+\frac{\partial rhV}{\partial r} = 0, \quad \rho h\left(\frac{\partial V}{\partial t}+V\frac{\partial V}{\partial r}\right) = \alpha\frac{\partial}{\partial r}\left(h\frac{\partial^2 h}{\partial r^2}\right). \tag{4.8a, b}$$

5. Capillary waves

Consider the propagation of small perturbations over a planar liquid film. The perturbations of the thickness and velocity are defined by the expressions

$$h = h_0[1+\chi(x,t)], \quad V = V_0[1+\beta(x,t)], \tag{5.1a, b}$$

where χ and β are much smaller than unity.

Substituting (5.1) in (4.5) and linearizing the governing equations, we arrive at

$$\frac{\partial\chi}{\partial t}+V_0\left(\frac{\partial\chi}{\partial x}+\frac{\partial\beta}{\partial x}\right)=0, \quad \rho V_0\left(\frac{\partial\beta}{\partial t}+V_0\frac{\partial\beta}{\partial x}\right)=\alpha h_0\frac{\partial^3\chi}{\partial x^3}. \tag{5.2a, b}$$

The wave-like solutions

$$\chi=\chi_0\exp(\mathrm{i}\omega t+\mathrm{i}kx), \quad \beta=\beta_0\exp(\mathrm{i}\omega t+\mathrm{i}kx) \tag{5.3a, b}$$

(where χ_0 and β_0 are some constants, ω is the angular frequency, and k is the wavenumber) readily yield a well-known dispersion relation (Whitham 1974, p. 405)

$$\omega=-kV_0\pm ak^2, \quad a=(\alpha h_0/\rho)^{1/2}. \tag{5.4a, b}$$

We can also consider a liquid layer to be at rest, until at $t=0$ a rather small perturbation is introduced at its centre (for example, by a drop falling from a small height or by a thin stick). In this case we assume V to be of the order of the perturbation, whereas for h expression (5.1 *a*) is used.

Linearizing equations (4.5), we obtain in the case studied here

$$\frac{\partial\chi}{\partial t}+\frac{\partial V}{\partial x}=0, \quad \rho\frac{\partial V}{\partial t}=\alpha h_0\frac{\partial^3\chi}{\partial x^3}, \tag{5.5a, b}$$

wherefrom we arrive at the following equations:

$$\frac{\partial^2\chi}{\partial t^2}+a^2\frac{\partial^4\chi}{\partial x^4}=0, \quad \frac{\partial^2 V}{\partial t^2}+a^2\frac{\partial^4 V}{\partial x^4}=0. \tag{5.6a, b}$$

Equations (5.6) represent a well-known beam equation. As $x\to\pm\infty$ the perturbation vanishes, $\chi\to 0$.

With a pointwise drop or stick as the source of the perturbation (which means that we study the remote asymptotics of the solution), the problem is self-similar and its solution should be sought in the form

$$\chi=f(\eta), \quad V=(a/t)^{1/2}\Phi(\eta), \quad \eta=x/(at)^{1/2}. \tag{5.7a–c}$$

As usual, we pose the following initial conditions:

$$t=0, \quad V=(a/t)^{1/2}S\delta(\eta), \quad \frac{\partial V}{\partial t}=0, \tag{5.8a, b}$$

where S is the non-dimensional perturbation 'strength'.

Self-similar solutions of (5.6) and (5.8) satisfy the equations

$$f^{\mathrm{iv}}+\tfrac{1}{4}\eta^2 f''+\tfrac{3}{4}\eta f'=0, \quad \Phi^{\mathrm{iv}}+\tfrac{1}{4}\eta^2\Phi''+\tfrac{5}{4}\eta\Phi'+\tfrac{3}{4}\Phi=0. \tag{5.9a, b}$$

The solution for large η is readily found, which yields the following wave trains:

$$\chi=\frac{S}{(2\pi)^{1/2}}\frac{1}{\eta}[\cos(\tfrac{1}{4}\eta^2)+\sin(\tfrac{1}{4}\eta^2)], \tag{5.10a}$$

$$V=\left(\frac{a}{t}\right)^{1/2}\frac{S}{2(2\pi)^{1/2}}[\cos(\tfrac{1}{4}\eta^2)+\sin(\tfrac{1}{4}\eta^2)]. \tag{5.10b}$$

The expression (5.10 *b*) is similar to that of Whitham (1974, p. 378). Solution (5.10) also corresponds to the initial perturbation of χ in the form

$$t=0, \quad \chi=S(\tfrac{1}{8}\pi)^{1/2}\delta(\eta). \tag{5.11}$$

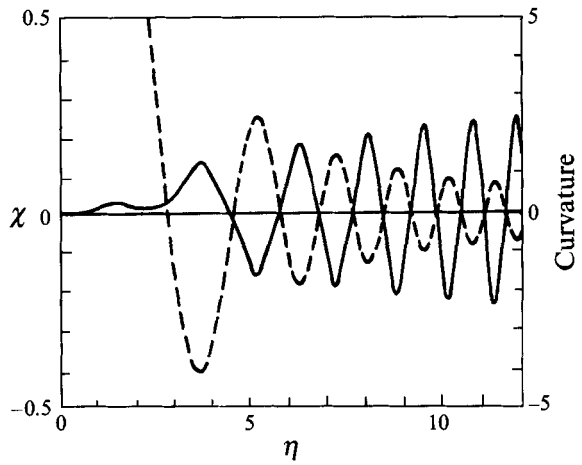

FIGURE 17. Calculated film thickness profile (– – –) and its curvature (——) for capillary waves according to (5.15*a*) with $S = \Gamma(\frac{1}{4})$.

In the axisymmetric case we obtain, correspondingly,

$$\frac{\partial^2 \chi}{\partial t^2} + \frac{a^2}{r}\frac{\partial}{\partial r}\left(r\frac{\partial^3 \chi}{\partial r^3}\right) = 0. \tag{5.12}$$

Equation (5.12) is similar to the equation for bending waves propagating over elastic plates (Landau & Lifshitz 1959, p. 111), albeit distinct from it.

In the axisymmetric case the self-similar solution is sought in the form of (5.7*a*, *b*) with

$$\eta = r/(at)^{1/2}, \tag{5.13}$$

and should satisfy the initial conditions (5.8). The equation for f reads

$$f^{\mathrm{iv}} + \frac{1}{\eta}f''' + \frac{\eta^2}{4}f'' + \frac{3}{4}\eta f' = 0. \tag{5.14}$$

Using the solution of (5.14), we find that for large η the axisymmetric waves are described by the following expressions:

$$\chi = \frac{2S}{\Gamma(\frac{1}{4})}\frac{1}{\eta^{3/2}}[\cos(\tfrac{1}{4}\eta^2 + \tfrac{1}{8}\pi) + \sin(\tfrac{1}{4}\eta^2 + \tfrac{1}{8}\pi)], \tag{5.15a}$$

$$V = \left(\frac{a}{t}\right)^{1/2}\frac{S}{\Gamma(\frac{1}{4})}\frac{1}{\eta^{1/2}}[\cos(\tfrac{1}{4}\eta^2 + \tfrac{1}{8}\pi) + \sin(\tfrac{1}{4}\eta^2 + \tfrac{1}{8}\pi)]. \tag{5.15b}$$

Solution (5.15) also corresponds to the following initial perturbation of χ:

$$t = 0, \quad \chi = 4\pi S\frac{\delta(\eta)}{2\pi\eta}. \tag{5.16}$$

For comparison with experiments profile (5.15*a*) is plotted together with its curvature in figure 17.

It is emphasized that capillary waves emerge only when the inertia forces on the left in the momentum equations (4.5) or (4.8) are of the same order of magnitude as the surface tension forces on the right, and they are in mutual competition.

6. Splashing as a kinematic discontinuity

Consider, first, the planar problem and rearrange the governing equations (4.5) to the following non-dimensional form:

$$\frac{\partial h}{\partial t}+\frac{\partial h V}{\partial x}=0, \quad h\left(\frac{\partial V}{\partial t}+V\frac{\partial V}{\partial x}\right)=\epsilon\frac{\partial}{\partial x}\left(h\frac{\partial^2 h}{\partial x^2}\right), \quad \epsilon=a^2f^2/V_0^4. \tag{6.1a–c}$$

Here, as before in §4, h_0 is used as a scale for h, V_0 for V, $1/f$ for t, and V_0/f for x.

We consider the limit of $\epsilon \ll 1$. Then the outer solution of the momentum equation (6.1*b*) satisfies the equation

$$\frac{\partial V}{\partial t}+V\frac{\partial V}{\partial x}=0, \tag{6.2}$$

which is solved in the following parametric form (Whitham 1974, p. 43):

$$V=F(\xi), \quad x=F(\xi)t+\xi. \tag{6.3a, b}$$

The function F describes an initial velocity distribution along the liquid layer, and ξ denotes the initial positions of the particles. This solution produces kinematic discontinuities in the function $V(x)$ ('shocks') in finite time if there is a ξ-interval for which $\mathrm{d}F/\mathrm{d}\xi<0$ holds.

To analyse the situation when such a discontinuity is formed, we write the continuity and momentum equations in the conservative form

$$\frac{\partial h}{\partial t}+\frac{\partial h V}{\partial x}=0, \quad \frac{\partial h V}{\partial t}+\frac{\partial h V^2}{\partial x}=0, \tag{6.4a, b}$$

whereas at the discontinuity the corresponding integral relations hold:

$$\frac{\mathrm{d}}{\mathrm{d}t}\int_{x_1}^{x_2} h\,\mathrm{d}x=h_-V_--h_+V_+, \quad \frac{\mathrm{d}}{\mathrm{d}t}\int_{x_1}^{x_2} hV\,\mathrm{d}x=h_-V_-^2-h_+V_+^2. \tag{6.5a, b}$$

Here $h_\pm$ and $V_\pm$ denote the thickness and velocity at $x=x_d\pm 0$ (x_d is the discontinuity position), and x_1 and x_2 are some fixed cross-sections of the film, $x_1<x_d<x_2$, close to the discontinuity at the given moment of time.

From (6.5) we arrive at the expressions for the velocity of the discontinuity $U_1=\mathrm{d}x_d/\mathrm{d}t$:

$$U_1=\frac{h_-V_--h_+V_+}{h_--h_+}=\frac{h_-V_-^2-h_+V_+^2}{h_-V_--h_+V_+}. \tag{6.6}$$

The last equality of (6.6) may be satisfied only if $V_-=V_+$, which is in contradiction with the fact that, owing to (6.3), a discontinuity in the velocity distribution V inevitably emerges if $\epsilon \ll 1$ and $\mathrm{d}F/\mathrm{d}\xi<0$ in some interval of the initial distribution. In the experiments performed and described above, the latter always happens with perturbations produced by subsequent drops impacting onto the solid surface, which is covered by a liquid layer.

The discontinuity in the velocity distribution emerges independently of the continuity equation; the only possibility for it to be realized in an *incompressible liquid* layer is related to a sink at its front. (It will be shown below that there has to be a sink rather than a source.) This sink is visualized as a liquid outflow along the discontinuity front into a thin sheet. The continuity and momentum equations are thus generalized to the following non-dimensional conservative form:

$$\frac{\partial h}{\partial t}+\frac{\partial h V}{\partial x}=Q_0\,\delta(x-x_d), \quad \frac{\partial h V}{\partial t}+\frac{\partial h V^2}{\partial x}=VQ_0\,\delta(x-x_d), \tag{6.7a, b}$$

where Q_0 is the sink strength, which may depend on time. Note that we continue to seek the outer solution, neglecting the surface tension effect as small compared to that of the inertia.

At the discontinuity the corresponding integral relations hold:

$$\frac{\mathrm{d}}{\mathrm{d}t}\int_{x_1}^{x_2} h\,\mathrm{d}x = h_- V_- - h_+ V_+ + \int_{x_1}^{x_2} Q_0\,\delta(x-x_d)\,\mathrm{d}x, \tag{6.8a}$$

$$\frac{\mathrm{d}}{\mathrm{d}t}\int_{x_1}^{x_2} hV\,\mathrm{d}x = h_- V_-^2 - h_+ V_+^2 + \int_{x_1}^{x_2} VQ_0\,\delta(x-x_d)\,\mathrm{d}x. \tag{6.8b}$$

From (6.8) we arrive at the following jump conditions at the discontinuity ($U = \mathrm{d}x_d/\mathrm{d}t$):

$$-U(h_+ - h_-) + h_+ V_+ - h_- V_- = Q_0, \tag{6.9a}$$

$$-U(h_+ V_+ - h_- V_-) + h_+ V_+^2 - h_- V_-^2 = V_d Q_0, \tag{6.9b}$$

where V_d is the velocity of the liquid at the discontinuity front. It should be equal to the centre-of-mass velocity

$$V_d = \frac{V_- h_- + V_+ h_+}{h_- + h_+}, \tag{6.10}$$

if we neglect viscous losses of momentum at the impingement of liquid particles entering the discontinuity from both sides.

By (6.9) and (6.10) we arrive at

$$U = \tfrac{1}{2}(V_- + V_+). \tag{6.11}$$

From (6.9a) and (6.11) we arrive at the following expression for the sink strength:

$$Q_0 = -\tfrac{1}{2}(h_+ + h_-)(V_- - V_+). \tag{6.12}$$

Since $V_- > V_+$, Q_0 is actually negative, which corresponds to a sink.

The equations describing the discontinuity position are readily obtained from (6.3) and (6.11) and have the form (Whitham 1974, p. 45):

$$x_d(t) = \xi_+ + F(\xi_+)\,t, \quad x_d(t) = \xi_- + F(\xi_-)\,t, \tag{6.13a, b}$$

$$\tfrac{1}{2}[F(\xi_+) + F(\xi_-)](\xi_+ - \xi_-) = \int_{\xi_-}^{\xi_+} F(\xi)\,\mathrm{d}\xi, \tag{6.13c}$$

with the unknowns x_d, ξ_+, and ξ_-.

An initial velocity distribution in the liquid film produced by a drop may be represented in the form of a single hump, schematically shown in figure 18. For such a distribution the system (6.13) has an asymptotic solution for sufficiently large t, when $F(\xi_+) = 0$ and $\xi_- \to 0$ (Whitham 1974, p. 47):

$$x_d(t) = (2At)^{1/2}, \quad A = \int_0^L F(\xi)\,\mathrm{d}\xi, \tag{6.14a, b}$$

which corresponds to

$$V_- = F(\xi_-) = (2A/t)^{1/2}, \quad V_+ = 0, \quad U = \tfrac{1}{2}(2A/t)^{1/2} \tag{6.15a–c}$$

(L is the dimensionless length of the hump).

Under this asymptotic regime the propagation of the discontinuity wave (identified by a crown-like sheet) depends on a single characteristic of the initial velocity distribution – its integral A in (6.14b).

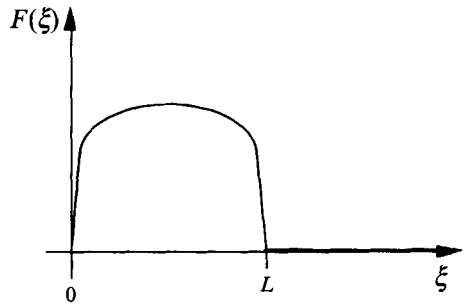

FIGURE 18. Initial velocity distribution in the layer created by drop impact. L is a scale related to the drop diameter.

Note that a hump may have a more complicated configuration than that of figure 18. First, in the general case it need not be symmetric. Second, there may be a slight wavyness in $F(\xi), 0 \leqslant \xi \leqslant L$. However, there should be a sharp decrease in $F(\xi)$ near $\xi = 0$ and $\xi = L$, similar to that of figure 18. This corresponds to the physical fact that there is a sharp boundary between the initial spot produced by a drop and a still unperturbed liquid layer outside it. All the results obtained hold for such a more complicated hump.

In the asymptotic regime considered, $V = F(\xi) = 0$ for all $\xi \geqslant \xi_+$. Therefore, $V \equiv 0$ at $x \geqslant x_d + 0$. At the same time, $\xi_- \to 0$, which means that to each $x \leqslant x_d - 0$ there corresponds a $\xi \leqslant \xi_- \ll 1$. For such small values of ξ the initial velocity distribution may be reduced to the first term of its Taylor series

$$F(\xi) = B\xi, \quad B > 0, \tag{6.16}$$

where the coefficient B is supposed to be known.

From (6.3*b*) and (6.16) we find

$$\xi = \frac{x}{1+Bt}, \quad V = \frac{Bx}{1+Bt}, \tag{6.17}$$

which describes the velocity profile to the left of the discontinuity, i.e. at $x \leqslant x_d - 0$.

From the continuity equation (4.5*a*) we obtain the following equation for h to the left of the discontinuity:

$$\frac{\partial h}{\partial t} + \frac{Bx}{1+Bt}\frac{\partial h}{\partial x} = -h\frac{B}{1+Bt}, \tag{6.18}$$

whereas to the right to the discontinuity

$$\frac{\partial h}{\partial t} = 0. \tag{6.19}$$

Therefore,

$$h = \begin{cases} \dfrac{1}{1+Bt}, & x < x_d, \\ 1 & x > x_d, \end{cases} \tag{6.20}$$

and we obtain the values of h at the discontinuity

$$h_- = \frac{1}{1+Bt}, \quad h_+ = 1. \tag{6.21\,a, b}$$

Note that (6.21*a*) is inapplicable in a certain interval of the intermediate values of t.

Expressions (6.21) show that the discontinuity propagates towards the thicker section of the liquid film, detaching a part of it in the manner of a cutter and propelling it towards the crown. Knowing V_-, V_+, h_- and h_+, we are able to calculate using (6.12) the volumetric flow rate to the crown Q_0 at any moment of time.

The condition of discontinuity (and, therefore, crown) formation, $\epsilon \ll 1$, may be rewritten as

$$V_0 \gg (\alpha/\rho)^{1/4} f^{1/2} h_0^{1/4}, \tag{6.22}$$

where h_0 is the unperturbed thickness of the liquid layer on the wall produced by preceding drops. In analogy with the original concept in gasdynamics, the ratio $V_0/(\alpha^{1/4}\rho^{-1/4}f^{1/2}h_0^{1/4})$ may in a sense be called a modified Mach number, and (6.22) means that it is much larger than unity. The same analogy is applicable to the ratio $V_0/(\alpha\rho^{-1}h_0^{-1})^{1/2}$ (i.e. the ratio of flow velocity to the characteristic propagation velocity of capillary waves) – under which definition (6.22) states that the modified Mach number is much larger than $(h_0/l)^{1/2}$, where l is the characteristic 'capillary length', $l = (\alpha/\rho h_0)^{1/2} f^{-1}$.

The liquid film on the wall is damped by the viscous forces. Therefore, its thickness is of the order of

$$h_0 \approx (\nu/f)^{1/2}. \tag{6.23}$$

Note that (6.23) predicts fairly well the order of magnitude of the film thickness estimated in §3.2. Indeed, for $\nu \sim 10^{-6}\ \mathrm{m^2\,s^{-1}}$ and $f \sim 10^4\ \mathrm{s^{-1}}$ (6.23) yields $h_0 \sim 10\ \mu\mathrm{m}$, whereas the estimated values vary between 20 and 50 μm.

Substituting (6.23) in (6.22) we arrive at the following estimate of the velocity range corresponding to splashing:

$$V_0 \gg (\alpha/\rho)^{1/4} \nu^{1/8} f^{3/8}. \tag{6.24}$$

It can readily be shown that all the above results are applicable to the axisymmetric case by simply replacing x with r. The only difference concerns the form of the sink. The continuity and momentum equations in the axisymmetric case take the form

$$\frac{\partial r h}{\partial t} + \frac{\partial r hV}{\partial r} = Qr, \quad \frac{\partial r hV}{\partial t} + \frac{\partial r hV^2}{\partial r} = VQr, \quad Q = Q_0 \frac{\delta(r - r_c)}{2\pi r}, \tag{6.25a–c}$$

where

$$Q_0/(2\pi r_c) = -\tfrac{1}{2}(h_+ + h_-)(V_- - V_+), \tag{6.26}$$

which should be used instead of (6.12). Note that here we have changed the subscript from d to c to stress the identification of the discontinuity with the crown. The velocity to the left of the sink under the asymptotic regime is $V = Br/(1 + Bt)$, and the equation for the thickness takes the form

$$\frac{\partial h}{\partial t} + \frac{Br}{1 + Bt}\frac{\partial h}{\partial r} = -h\frac{2B}{1 + Bt}. \tag{6.27}$$

Its solution reads $h = (1 + Bt)^{-2}$ at $r < r_c$, which means that

$$h_- = \frac{1}{(1 + Bt)^2}, \quad h_+ = 1. \tag{6.28a, b}$$

The latter should be used instead of (6.21).

7. Structure of the discontinuity wave

Within the framework of the quasi-one-dimensional model used here, we are unable to account for the two-dimensional effects inside the discontinuity. By applying this model here, we mimic the internal structure of the discontinuity and prove that it

matches the outer solution found in §6. We first address the planar case. Bearing in mind (6.1) and (6.7), we arrive at the following non-dimensional equations for the structure of the discontinuity:

$$\frac{\partial h}{\partial t}+\frac{\partial h V}{\partial x}=Q_0\,\delta(x-x_d),\quad h\left(\frac{\partial V}{\partial t}+V\frac{\partial V}{\partial x}\right)=\epsilon\frac{\partial}{\partial x}\left(h\frac{\partial^2 h}{\partial x^2}\right). \tag{7.1a, b}$$

Inside the discontinuity the singular right-hand side of the momentum equation (7.1*b*) should survive as $\epsilon\to 0$, which means that the inner stretched variable should be taken as

$$X=(x-x_d(t))/\epsilon^{1/2}. \tag{7.2}$$

As a distributed delta-function inside the discontinuity as $\epsilon\to 0$ we use, for example,

$$\delta(x-x_d)=\frac{1}{\epsilon^{1/2}\pi^{1/2}}\exp\left[-\frac{1}{\epsilon}(x-x_d)^2\right]. \tag{7.3}$$

By means of (7.1)–(7.3), bearing in mind that $U=\mathrm{d}x_d/\mathrm{d}t$, we arrive at the inner equations

$$\frac{\partial h(V-U)}{\partial X}=\frac{Q_0}{\pi^{1/2}}\exp(-X^2),\quad h(V-U)\frac{\partial V}{\partial X}=\frac{\partial}{\partial X}\left(h\frac{\partial^2 h}{\partial X^2}\right) \tag{7.4a, b}$$

with time only a parameter, introduced through the boundary conditions. Equations (7.4) mimic the effect of liquid outflow somewhere inside the discontinuity wave.

The matching conditions for the solution of (7.4) read

$$h\to h_-,\quad V\to V_-\quad\text{as}\quad X\to-\infty, \tag{7.5a, b}$$

$$h\to h_+,\quad V\to V_+\quad\text{as}\quad X\to+\infty, \tag{7.5c, d}$$

whereas all the derivatives of h and V tend to zero as $X\to\pm\infty$.

To prove that a solution of (7.4) satisfies the matching conditions as $X\to-\infty$, we take

$$h=h_-[1+\chi(X)],\quad (V-U)=(V_--U)[1-\beta(X)], \tag{7.6a, b}$$

$$\chi,\quad \beta\ll 1, \tag{7.6c, d}$$

which enables us to linearize the problem at the edge $X\to-\infty$ of the discontinuity structure.

From (7.4*a*) and (7.6) we obtain

$$\chi-\beta=\frac{Q_0}{2A_-}[1+\mathrm{erf}(X)],\quad A_-=h_-(V_--U). \tag{7.7a, b}$$

Substituting (7.7) in (7.4*b*), linearizing and integrating once, we arrive at the equation:

$$\frac{\partial^2\beta}{\partial X^2}+M^2\beta=NX\exp(-X^2),\quad M^2=\frac{(V_--V_+)^2}{4h_-},\quad N=\frac{2Q_0}{A_-\pi^{1/2}}. \tag{7.8a–c}$$

The solution of (7.8*a*) satisfying (7.5) reads

$$\beta=-\frac{N}{2}\left\{\sin(MX)\int_{-\infty}^{X}\exp(-\xi^2)\sin(M\xi)\,\mathrm{d}\xi+\cos(MX)\int_{-\infty}^{X}\exp(-\xi^2)\cos(M\xi)\,\mathrm{d}\xi\right\}, \tag{7.9}$$

whereas all the derivatives tend to zero as $X\to-\infty$.

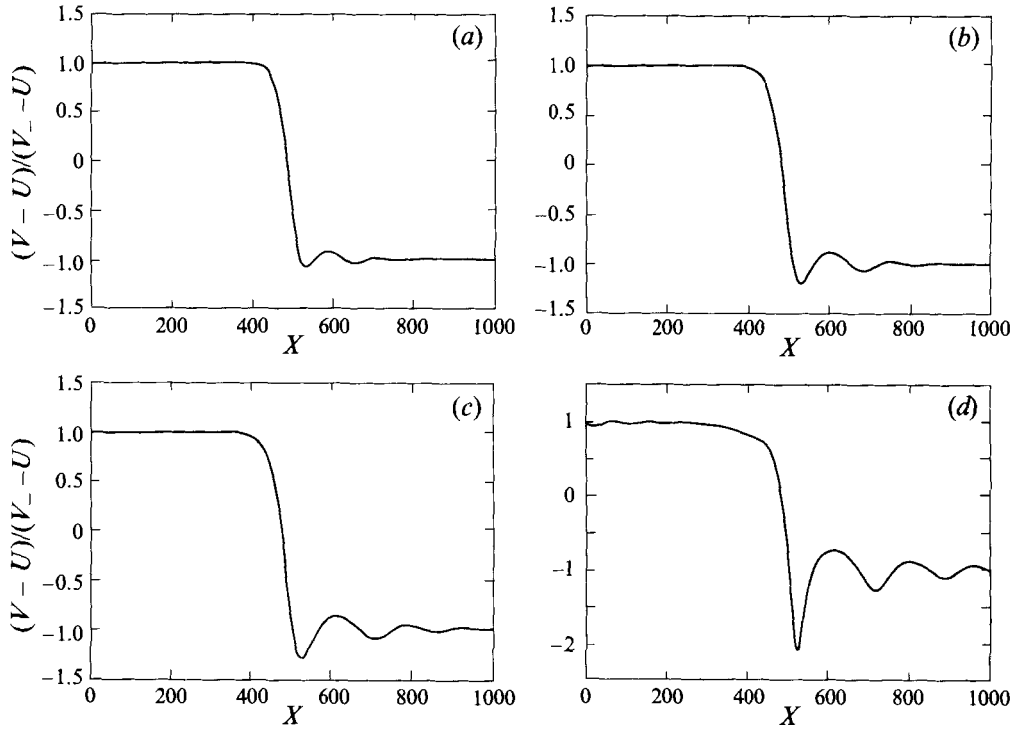

FIGURE 19. Internal structure of the discontinuity. (*a*) $M = 1$, $N = -4$; (*b*) $M = 1$, $N = -5$; (*c*) $M = 1$, $N = -6$; (*d*) $M = 1.5$, $N = -4$.

The solution at the right-hand edge of the discontinuity structure is obtainable similarly and reads

$$h = h_+[1-\chi_1(X)], \quad (V-U) = (V_+-U)[1-\beta_1(X)], \tag{7.10a, b}$$

$$\chi_1, \quad \beta_1 \ll 1, \tag{7.10c, d}$$

$$\beta_1 = -\frac{N_1}{2}\left\{\sin(M_1 X)\int_\infty^X \exp(-\xi^2)\sin(M_1\xi)\,d\xi + \cos(M_1 X)\int_\infty^X \exp(-\xi^2)\cos(M_1\xi)\,d\xi\right\}, \tag{7.10e}$$

$$M_1^2 = \frac{(V_+-V_-)^2}{4h_+}, \quad N_1 = \frac{2Q_0}{A_+\pi^{1/2}}, \quad A_+ = h_+(V_+-U). \tag{7.10f–h}$$

The latter satisfies all the matching conditions as $X \to \infty$.

A continuous solution of (7.4) and (7.5) is found numerically and shown in figure 19. Note a wavyness in the velocity distribution before the discontinuity.

In the axisymmetric case we obtain instead of (7.4) the following equations:

$$\frac{\partial h(V-U)}{\partial X} = \frac{Q_0}{2\pi r_c}\frac{1}{\pi^{1/2}}\exp(-X^2), \quad h(V-U)\frac{\partial V}{\partial X} = \frac{\partial}{\partial X}\left(h\frac{\partial^2 h}{\partial X^2}\right), \tag{7.11a, b}$$

where the stretched coordinate is

$$X = (r-r_c(t))/\epsilon^{1/2}. \tag{7.12}$$

Equations (7.11) show that all the results of the planar case hold in the axisymmetric one on replacing Q_0 with $Q_0/(2\pi r_c)$.

8. Comparison with experiment, and discussion

First the capillary waves obtained in the experiment (§3.1) are compared with the theoretical wave pattern predicted in §5. To this end the curvature of the film profile according to (5.1*a*) and (5.15*a*) was determined (see figure 17). Its maxima (corresponding to depressions in the wave profile) are expected to yield dark rings in the experiment (cf. figure 4), since a liquid film has the effect of a dispersing lens in the depressions. We plot the values of η corresponding to the curvature maxima, $\eta_i (i = 1, 2, \ldots)$, as the horizontal lines in the $\eta(r)$ diagram in figure 20. (The maximum of the curvature at $\eta \approx 1.44$ has little physical sense, since $|\chi| \ll 1$ is not fulfilled there.) The measured radii of the dark rings are plotted as the vertical lines in the same figure. As can be seen in figure 20, the intersection points of corresponding pairs of vertical and horizontal lines lie on a straight line. Its slope is $\Delta\eta/\Delta r \approx 937\ \mathrm{m}^{-1}$.

The theory also predicts $\eta(r)$ dependence, corresponding to the depressions of the wave profile, in the form of a straight line (cf. (5.13)). For a time delay after impact of $t \approx 5$ ms, one obtains from (5.13) $\Delta\eta/\Delta r = 1/(at)^{1/2} = t^{-1/2}(\alpha h_0/\rho)^{-1/4} = 995\ \mathrm{m}^{-1}$ ($\alpha = 23 \times 10^{-3}\ \mathrm{kg\ s}^{-2}$; $\rho = 790\ \mathrm{kg\ m}^{-3}$, $h_0 = 1.4 \times 10^{-3}$ m), which agrees fairly well with the above value of $\Delta\eta/\Delta r = 937\ \mathrm{m}^{-1}$ found in the experiment.

The fact that the straight line in figure 20 does not hit the origin is interpreted as a result of a shift in r inevitably appearing when a remote asymptotic solution is fitted to an initial flow region. In a sense the introduction of such a shift is similar to that of the 'polar distance', required when comparing, for example, a self-similar solution for laminar or turbulent jets (Schlichting 1979; Abramovich 1963) with experimental data obtained for a jet issuing from an orifice. Nonlinear effects, which perhaps, affect the initial development of the wave train, may also lead to such a shift.

The theoretical prediction of the velocity range for splashing in the form of the inequality (6.24) should be compared with the experimental threshold velocity, which was established in the experiment in §3.2 and may be rearranged to the following form:

$$V_{0s} = 18(\alpha/\rho)^{1/4}\, \nu^{1/8} f^{3/8}. \tag{8.1}$$

It is seen that the theoretical result (6.24) predicts exactly the same scaling as in (8.1), and agreement is rather good.

It is interesting to compare the splashing criterion obtained here with that for a single drop impacting a dry surface known from the literature. Several authors, e.g. Stow & Hadfield (1981), mention $We\, Re^{1/2}$ (or a power of it) as the relevant dimensionless number for splashing ($We = \rho D V_0^2/\alpha$ is the Weber number and $Re = V_0 D/\nu$ is the Reynolds number). Notice that the relative power of viscosity, density and surface tension is the same in both cases. Indeed, (8.1) may be recast in the form $V_{0s}^8 = \text{const} \times (\alpha/\rho)^2 \nu f^3$, and the criterion of Stow & Hadfield (1981) in the form $V_{0s}^8 = \text{const} \times (\alpha/\rho)^2 \nu (V_0/D)^3$. Thus one is led to substitute f by V_0/D in the case of single drop impact and also to take $(\nu D/V_0)^{1/2}$ as a scale for the liquid lamella thickness h_0. This corresponds to the assumption that the characteristic time in single-drop impact is D/V_0. In this way the scaling behaviour for the single-drop impact would be reproduced.

As first approximation of the initial velocity distribution on impact we use

$$F(\xi) = \begin{cases} V_0, & 0 \leqslant \xi \leqslant R, \\ 0, & \xi > R, \end{cases} \tag{8.2}$$

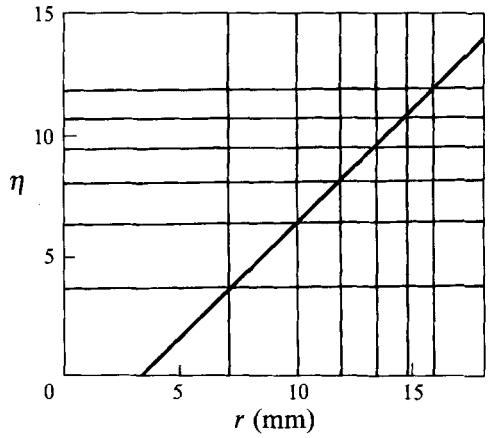

FIGURE 20. Capillary waves: comparison between the experiment and theory (§§3.1 and 5, respectively). Dark rings were measured at the drawn radii (vertical lines); they correspond to η-values where the profile (5.15a) has maximum curvature (horizontal lines).

where R is the radius of the initial spot in the centre of the film produced by a drop. Note that we neglect momentum losses on impact. We can estimate R from the mass balance

$$\rho\pi R^2 h_0 = \tfrac{1}{6}\rho\pi D^3, \tag{8.3}$$

where D is the drop diameter. Recalling (6.23) we arrive at

$$R = kD, \quad k = (D/6)^{1/2}/(\nu/f)^{1/4}. \tag{8.4a, b}$$

The value of L corresponding to (6.14b) is $L = Rf/V_0 = kDf/V_0$. This is also the value, in the case here, of A in (6.14b) and (6.15). Therefore (6.14a) takes the form

$$\frac{r_c}{D} = \left(\frac{kV_0}{\pi Df}\right)^{1/2}\tau^{1/2} = \frac{V_0^{1/2}}{6^{1/4}\pi^{1/2}\nu^{1/8}D^{1/4}f^{3/8}}\tau^{1/2}, \tag{8.5}$$

where $\tau = 2\pi ft$ is non-dimensional time (t being the dimensional time). Note that here we adapt the definitions of the non-dimensional values of §6 to those of the experiment.

Equation (8.5) describes the position of the crown (a liquid sheet virtually normal to the wall) during its propagation with the discontinuity as a function of time. It should be emphasized that (8.5) predicts the square-root dependence on time (on the phase τ), in good agreement with the experimental approximations of (3.1). In the experiment, however, the moment of impact and the initial spot formation are not known exactly and time is reckoned from an instant known typically up to a precision of about 0.1 on the τ-scale. This, as well as in particular the fact that the experimental results are compared with theoretical predictions of the asymptotic solutions, brings in the shifting factor τ_0; therefore we should rewrite (8.5) in a form similar to (3.1) and (3.2):

$$\frac{r_c}{D} = \frac{V_0^{1/2}}{6^{1/4}\pi^{1/2}\nu^{1/8}D^{1/4}f^{3/8}}(\tau-\tau_0)^{1/2}. \tag{8.6}$$

In a sense the introduction of τ_0 is similar to that of the 'polar distance' discussed above. The theoretical predictions of (8.6) in the cases corresponding to (3.1a–c) take the form

$$r_c/D = 1.18(\tau-1.54)^{1/2}, \quad r_c/D = 1.24(\tau-1.38)^{1/2}, \quad r_c/D = 1.29(\tau-1.28)^{1/2} \tag{8.7a–c}$$

and are plotted in figure 11(a–c) against the experimental data.

Comparison of the above predictions with (3.1*a–c*) shows fairly close agreement, with the theoretical values of r_c/D consistently overestimated. This is due to our exclusion of the momentum losses at the moment of impact, when the effect of viscosity is inevitably significant because of the large velocity gradients involved. We use in (8.2) and (8.5)–(8.7) the impact velocity V_0 as an estimate of the initial velocity in the accelerated spot in the centre of film, while, in reality the impact losses dictate a lower value, thereby shifting (8.7) towards the experimental data.

The square-root behaviour according to (8.5) can also be found in the results of Levin & Hobbs (1971) obtained for single-drop impact onto a quite thick liquid film of a given thickness h_0. To compare their results one has to set $k = [D/(6h_0)]^{1/2}$ and $f = V_0/D$, which leads to

$$\frac{r_c}{D} = \left(\frac{2}{3}\right)^{1/4} \frac{V_0^{1/2}}{D^{1/4}h_0^{1/4}}(t-t_0)^{1/2}. \tag{8.8}$$

For $V_0 = 4.8\ \mathrm{m\ s^{-1}}$, $D = 2.9 \times 10^{-3}$ m and $h_0 = 0.5 \times 10^{-3}$ m and shifting time $t_0 = 0.536 \times 10^{-4}$ s (obtained by fitting the first experimental point in figure 9 of Levin & Hobbs (1971) by (8.8)) we find from (8.8)

$$r_c = 165.3 \times 10^{-3}(t-t_0)^{1/2}, \tag{8.9}$$

which describes fairly well the experimental data in figure 9 of Levin & Hobbs (1971) with an overestimation of 11–19 %. The overestimation may be attributed partly to the effect of the rather thick liquid film which gives rise to a significant velocity component normal to the wall.

As mentioned in §3, the compressibility effects do not affect the splashing threshold, which shows that they are 'forgotten' in the timescale of the whole process. Indeed, according to Bowden & Field (1964), under the conditions of the present experiment the compressibility effects are of importance before the radius of the contact periphery of a drop reaches a value of $r_0 \approx DV_0/(2c)$, where c is the compressional velocity for the liquid. For $c \sim 10^3\ \mathrm{m\ s^{-1}}$, $V_0 \sim 10\ \mathrm{m\ s^{-1}}$ and $D \sim 300\ \mu$m we obtain $r_0 \sim D/200 = 1.5\ \mu$m. The compressed region at the bottom of the drop will be rarefied by a release wave; then sideways jetting begins. The time needed for jetting to begin can be estimated as $r_0/c = DV_0/(2c^2)$, which is of the order of 1.5×10^{-9} s for the present experiment. Beginning from this moment the flow may be treated as incompressible.

The characteristic time of splashing in the present experiment is $(2\pi f)^{-1} \sim 10^{-5}$ s (it corresponds to $\Delta\tau = 1$ in figure 11). Since $(2\pi f)^{-1} \gg r_0/c$, the flow becomes incompressible almost immediately in the timescale of the splashing process as a whole (crown propagation and breakup).

Much more time is needed for a drop to create the initial spot in the centre of the film. This time is of the order of $D/V_0 \sim 3 \times 10^{-5}$ s, which corresponds to $\tau \sim 3$ in figure 11. The crown emerges and begins to propagate slightly before this moment. The velocity in the initial spot is of the order of V_0 since the losses appear to be negligible (Levin & Hobbs 1971). In a sense the time lag needed for the initial spot formation is partially absorbed in τ_0.

In figure 8 it is seen that the effect of surface roughness on the splashing threshold is practically negligible in the present experiment – the data for $R_z = 1$ and 16 μm are grouped together. Stow & Hadfield (1981) found that for a single drop surface roughness does not affect significantly the critical impact velocity for splashing if it is not at least two or three orders of magnitude smaller than the drop diameter. Stow & Stainer (1977) showed that surface roughness has a small effect on splashing when it

is varied beneath a liquid layer at the wall. Our experimental conditions fit this case: $R_z = 1$ or 16 μm, and $h_0 \sim (\nu/f)^{1/2} \sim 20$ to 50 μm is larger than the roughnesses. Thus our conclusion about the independence of the results of surface roughness is consistent with the results of Stow & Stainer (1977) and Stow & Hadfield (1981).

Kinematic discontinuities in thin liquid layers on a solid surface may emerge owing to the effect of centrifugal force in spin coating of Newtonian and power-law liquids (Emslie, Bonner & Peck 1958; Acrivos, Shah & Petersen 1960), or owing to the concentrational Marangoni effect in Marangoni drying (Jensen & Grotberg 1992; O'Brien 1993). In both of these cases the inertia of the liquid may be neglected in comparison with the viscous shear force acting in the thin liquid layer (lubrication approximation), which allows one to arrive at a quasi-one-dimensional equation of the evolution of the layer thickness. (A similar approach is used e.g. in Sharma & Ruckenstein 1988, Hwang & Ma 1989, and Yarin, Oron & Rosenau 1993, and allows one to account for surface tension, gravity and some other effects.) This equation for the layer thickness is similar to (6.2) under the conditions when surface tension and gravity are negligible, and yields the emergence of a jump in the film thickness.

It should be noted that in the present case of splashing, the inertia of the liquid layer is accounted for and, being much larger than surface tension, leads to the emergence of a kinematic discontinuity in the velocity field manifesting itself in crown formation.

Most of the results on the emergence of kinematic discontinuities in spin coating, Marangoni drying, and in the present case of splashing, are obtained in the framework of the quasi-one-dimensional equations. Such equations are relevant even in the cases when a discontinuity sets in, since the film outside the discontinuity continues to be smooth enough, whereas consideration of the discontinuity is separated by jump conditions. Nevertheless, a much more complete (and complicated) two-dimensional analysis is desirable. A two-dimensional model might also be useful in the present case to match the outer inviscid splashing solution with the model of viscous flow in the neighbourhood of the moving ejection line shown in figure 6 of Peregrine (1981).

Consider now the breakup of the crown top leading to the formation of secondary droplets. At the top of the crown surface tension forces create a motion of liquid towards the wall. As a result a swell in the form of a rim emerges and moves over the crown to the wall, sucking in new liquid. The speed of propagation of such a rim was calculated by Taylor (1959) as $V_* = [2\alpha/(\rho\delta)]^{1/2}$, where δ is the crown wall thickness. In a sense such a rim is similar to a toroidal cylinder and, in principle, may be subject to capillary instability due to the growth of longitudinal perturbations leading to a reduction of its surface area and breakup. This scenario, similar to the capillary breakup of thin free jets (Rayleigh 1878), does not agree, however, with the experimental evidence in the given case. Indeed, according to our measurements the crown wall thickness $\delta \lesssim D/15$. Estimating the lowest value of the rim cross-section radius at the top of the crown as $\delta/2 = D/30$, we arrive at the wavelength of the fastest growing perturbation $\lambda_* = 2\pi(\delta/2)/0.698 = 9\delta$ (low-viscosity liquids, Rayleigh 1878 and Yarin 1993, p. 2). The length of the toroidal cylinder (rim) $L = 2\pi r_c$. Thus the number of droplets produced by the rim is $n = L/\lambda_* = 2\pi r_c/(9D/30)$. According to figure 9 of Levin & Hobbs (1971) $L \approx 4$ mm at the moment of crown emergence when perturbations set in; the drop diameter $D = 2.9$ mm and thus the number of secondary droplets emerging simultaneously from the rim $n \approx 5$. It should be noted that the value of n is overestimated since we underestimate the rim cross-section radius and do not account for a stabilization of a jet (in the case here, a rim) by stretching (Taylor 1934; Tomotika 1936; Mikami, Cox & Mason 1976; Khakhar & Ottino 1987). (The rim is stretched when the crown wall propagates outwards from the point of drop impact.)

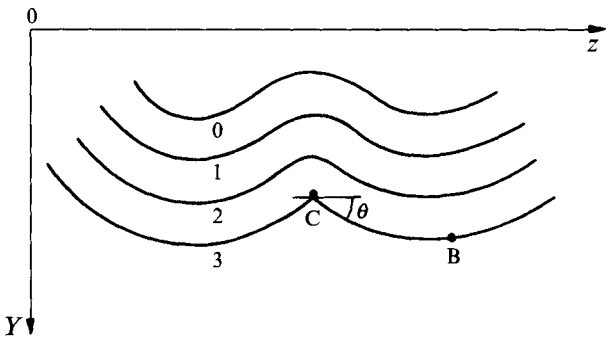

FIGURE 21. Cusp formation in the free rim at the top of the crown. Numeral 0 marks the initial configuration of the rim axis; 1 and 2 show intermediate configurations, whereas at 3 the cusp appears at point C. The crown wall is always below the rim in the figure. A thin jet from the cusp will be issued in the negative direction of the Y-axis leading to formation of secondary droplets (due to its breakup) above the crown (cf. figure 1*b*).

Even this overestimated value of n is much smaller than the number of jets issuing upwards from the top of the crown shown in figure 8 of Levin & Hobbs (1971) which is approximately equal to 10 on the half of the crown seen in the photograph. The overall number of secondary droplets emerging simultaneously from the crown rim in the experiment is of the order of 20, whereas the prediction based on the assumption that the breakup results from the capillary instability of the rim yields $n = 5$. The latter shows that such a scenario does not hold.

We can arrive at the same conclusion using the data obtained in the present experiment. From figure 14 we obtain the mean secondary droplet diameter to be of the order of $d = 0.06D$. One main secondary droplet is produced per wavelength along the free rim, considered as a jet in the process of capillary breakup. Thus $\pi(\delta/2)^2\lambda_* = \pi d^3/6$, which yields for $\delta/2 = D/30$ the value of $\lambda_* = 0.0324D$. The number of simultaneously emerging secondary droplets is, thus, $n = 2\pi r_c/\lambda_* = (2\pi/0.0324)r_c/D$. The value of r_c/D is close to unity at the moment of crown emergence (figure 11). Therefore $n \approx 200$, which is an order of magnitude higher than the real number of secondary droplets per rim circumference in the present experiment (see figure 16).

On the photographs in figure 8 of Levin & Hobbs (1971), as well as on many other photographs of breaking liquid films, it is clearly seen that the formation of droplets begins from cusps on the free rim. Such cusps inevitably result from the dynamics of a free rim (Yarin 1993, pp. 27–28). Indeed, the configuration of the free rim is governed by the equation

$$\frac{\partial Y}{\partial t} = V_*\left[1+\left(\frac{\partial Y}{\partial z}\right)^2\right]^{1/2} \tag{8.10}$$

which simply expresses the fact that the rim propagates normally to its instantaneous configuration with the speed $V_* = [2\alpha/(\rho\delta)]^{1/2}$ (Y- and z-axes are depicted in figure 21). The reference frame is 'frozen' in the film far enough from the rim.

This equation is solved under the initial condition $t = 0$, $Y = Y_0(z)$ describing an initial perturbed (if $Y_0 \neq$ const) form of the rim (see figure 21). Equation (8.10) is the eikonal equation which is solved by integration along its characteristic curves (Whitham 1974, pp. 241–242). This is identical with the Huygens principle applied to construct solutions in geometrical optics and combustion theory (Whitham 1974; Zeldovich *et al.* 1985). An example of a solution of (8.10) is shown in figure 21, where the initial configuration of the rim axis (marked by 0; the crown wall is below it)

arrives, via some intermediate configurations (marked 1 and 2), at the configuration with a cusp (3) at point C. At this cusp two neighbouring sections of the free rim impinge. As a result a thin jet originates from the cusp, which breaks up into secondary droplets under the action of surface tension forces (Yarin 1993, pp. 27–28). It is evident that the number of such jets (as well as cusps) producing secondary droplets is governed by the source of initial perturbations (details of drop impact, surface roughness, etc.) and may be large because one cusp corresponds to each convex section of the initial rim.

A cusp propagates with a velocity $V_*/\cos\theta$, faster than point B propagating with a velocity V_* (angle θ and point B are shown in figure 21). Therefore the cusp amplitude A_c decreases as $\mathrm{d}A_c/\mathrm{d}t \approx -V_*(1/\cos\theta - 1)$ leading to the less pronounced pattern of figure 16 of the present work than that of figure 8 of Levin & Hobbs (1971).

Note that in the general case disturbances of the top of the crown are non-axisymmetric. Therefore the crown may break up in different ways on different sides, as is seen in figure 10(*c*). The presence of these non-axisymmetric disturbances of the rim may have an effect on flow inside the crown and lamella. However, above we assumed that the rim does not affect the flow in the crown and lamella. This assumption rests on two facts. First, the liquid always flows from the crown to the rim (the reverse flow is not seen in experiments with free rims at the edges of the free films; Yarin 1993, p. 256). Secondly, only fairly rapid flows are considered in which perturbations are propagated mostly along the flow.

The secondary droplet size distributions shown in figure 14, with bumps at larger values of d/D as well as their global maximum at $d/D \approx 0.06$, cannot be represented accurately by the log-normal distribution function employed by Stow & Stainer (1977) for single-drop impact. Probably these bumps result from nonlinear effects leading to satellite droplet formation in the capillary breakup of thin jets issuing from the cusps.

Speculating on the effect of an increase in the dimensionless impact velocity u, one might expect that these bumps will disappear completely owing to further chaotization of flow in the lamella, crown and thin jets. One of the existing models of chaotic disintegration of a liquid mass (e.g. the percolation model of Sultanov & Yarin 1990 and Yarin 1993, pp. 338–348, or the combinatorial model of Cohen 1991) might be useful in future for an analysis of droplet size distributions after a drop impact.

Under the assumption that the asymptotic stage of splashing for large t considered in §6 has the dominant effect on the result, it should in principle be possible to estimate analytically the total volume of secondary droplets. Using (6.26), (6.14), (6.15), (8.4*b*), and the expression $A = kDf/V_0$ obtained above in the present Section, we arrive at the expression

$$W = \frac{|Q_0|}{\pi D^3/6} = \frac{(24)^{1/2} V_0 \nu^{1/4}}{D^{3/2} f^{1/4}}. \tag{8.11}$$

Here W is the total volume of the droplets per unit time in units of drop volume. Unfortunately, the actual duration of their generation in the process of crown propagation is unknown and only the onset of mass ejection can be estimated roughly. Extrapolating the straight line in figure 13 backwards to $h_c = 0$, we obtain the starting point at $r_c/D \approx 0.23$. From this we arrive, via figure 11(*b*), at $\tau = 1.4$ as starting value for the ejection onset phase. This estimate is not very sensitive to the uncertainties in the value of r_c/D due to the infinite slope of the curves at $\tau = \tau_0$ in figure 11, but still does not enable us to obtain via (8.11) data for comparison with the experimental results plotted in figure 15.

9. Conclusions

Self-similar capillary waves were measured experimentally and calculated analytically. It was confirmed that the relevant variable in the liquid film is $\eta = r/(at)^{1/2}$. The measured maxima of the film surface curvature fit well those of the calculated profile.

The impact of drop trains on solid surfaces was investigated experimentally and theoretically. A quasi-one-dimensional model was developed for the flow in the liquid lamella on the wall. The model predicts the existence of a new type of kinematic discontinuity wave, namely a discontinuity in the velocity and film-thickness distributions. This discontinuity shows many aspects of a shock wave, but also propagates in an *incompressible liquid*. The discontinuity has a sink of mass at its front, which corresponds to the emergence of a thin liquid sheet parallel to the discontinuity front and virtually normal to the film on the wall. This sheet propagates outwards from the point of drop impact together with the discontinuity, and is identified with the crown accompanying splashing in the experiments. This crown is unstable owing to the formation of a free rim at its top, which results in cusps from which thin jets emerge. Capillary breakup of the jets leads to the formation of a cloud of secondary droplets.

The kinematic discontinuity wave in splashing is essentially different from a hydraulic jump, since the dominating forces, besides the inertial ones, are capillary rather than gravitational.

The model predicts the emergence of the kinematic discontinuity wave and splashing at $\epsilon = \alpha\nu^{1/2}f^{3/2}/(\rho V_0^4) \ll 1$ (α is the surface tension coefficient, ν the kinematic viscosity, f the frequency, ρ the density, and V_0 the impact velocity). Experimental results permit a quantitative statement: splashing emerges if $\epsilon \lesssim 18^{-4}$. From this it can be seen that surface tension is the dominant damping force. The internal structure of the kinematic discontinuity wave is discussed.

The emergence of similar kinematic discontinuity waves in incompressible liquid flows with free surfaces may be predicted in some other situations. For example, in free liquid jets of relatively large radius with strong pulsations in the issue velocity imposed by a piston, crowns similar to those of splashing can clearly be seen along the jet axis in figure 7(*c*) in Meier, Klöpper & Grabitz (1992). They appear for the same reason as in drop impact, since the quasi-one-dimensional momentum equation for liquid jets with inertia dominating over surface tension takes the form of (6.2) (Yarin 1993).

A.L.Y. is a recipient of the Guastalla Fellowship established by the Fondation Rashi, and the Planning and Grants Committee of the Council of Higher Education of the Israel Academy of Sciences and Humanities. He is also indebted to the Bezirksregierung Braunschweig, Volkswagen-Stiftung for financial assistance and to the Max-Planck-Institut für Strömungsforschung in Göttingen for their hospitality in 1992 and 1993. D.A.W. is indebted to Dr H. Chaves, Dr F. Feuillebois, Professor F. Obermeier, and Dr M. Rein for many helpful and stimulating discussions and to Dipl. Phys. W. Hiller, Dr T. Kowalewski, and Dipl. Phys. K. Range for useful advice; financial support by CEC and JRC as well as by Schweizerischer Nationalfonds is gratefully acknowledged.

REFERENCES

ABRAMOVICH, G. N. 1963 *The Theory of Turbulent Jets*. The MIT Press.

ACRIVOS, A., SHAH, M. J. & PETERSEN, E. E. 1960 On the flow of a non-Newtonian liquid on a rotating disk. *J. Appl. Phys.* **31**, 963.

ALLEN, R. F. 1975 The role of surface tension in splashing. *J. Colloid Interface Sci.* **51**, 350.

ALLEN, R. F. 1988 The mechanics of splashing. *J. Colloid Interface Sci.* **124**, 309.

BOWDEN, F. P. & FIELD, J. E. 1964 The brittle fracture of solids by liquid impact, by solid impact, and by shock. *Proc. R. Soc. Lond.* A **282**, 331.

COHEN, R. D. 1991 Shattering of a liquid drop due to impact. *Proc. R. Soc. Lond.* A **435**, 483.

EMSLIE, A. G., BONNER, F. T. & PECK, L. G. 1958 Flow of a viscous liquid on a rotating disk. *J. Appl. Phys.* **29**, 858.

ENGEL, O. G. 1955 Waterdrop collisions with solid surfaces. *J. Res. Natl. Bureau Stand.* **54**, 281.

FANTINI, E., TOGNOTTI, L. & TONAZZINI, A. 1990 Drop size distribution in sprays by image processing. *Computers Chem. Engng* **14**, 1201.

FUKAI, J., ZHAO, Z., POULIKAKOS, D. & MEGARIDIS, C. M. 1993 Modeling of the deformation of a liquid droplet impinging upon a flat surface. *Phys. Fluids* A **5**, 2588.

HARLOW, F. H. & SHANNON, J. P. 1967 The splash of a liquid drop. *J. Appl. Phys.* **38**, 3855.

HWANG, J. H. & MA, F. 1989 On the flow of a thin liquid film over a rough rotating disk. *J. Appl. Phys.* **66**, 388.

JENSEN, O. E. & GROTBERG, J. B. 1992 Insoluble surfactant spreading on a thin viscous film: shock evolution and film rupture. *J. Fluid Mech.* **240**, 259.

KHAKHAR, D. V. & OTTINO, J. M. 1987 Breakup of liquid threads in linear flows. *Intl. J. Multiphase Flow* **13**, 71.

LABEISH, V. G. 1994 Thermodynamic study of a drop impact against a heated surface. *Expl. Thermal Fluid Sci.* **8**, 181.

LANDAU, L. D. & LIFSHITZ, E. M. 1959 *Theory of Elasticity*. Pergamon.

LESSER, M. B. 1981 Analytic solutions of liquid-drop impact problems. *Proc. R. Soc. Lond.* A **377**, 289.

LESSER, M. B. & FIELD, J. E. 1983 The impact of compressible liquids. *Ann. Rev. Fluid Mech.* **15**, 97.

LEVIN, Z. & HOBBS, P. V. 1971 Splashing of water drops on solid and wetted surface: hydrodynamics and charge separation. *Phil. Trans. R. Soc. Lond.* A **269**, 555.

LINDBLAD, N. R. & SCHNEIDER, J. M. 1965 Production of uniform-sized liquid droplets. *J. Sci. Instrum.* **42**, 635.

LIU, X. & LIENHARD, V. J. H. 1993 The hydraulic jump in circular jet impingement and in other thin liquid films. *Exp. Fluids* **15**, 108.

LOEHR, K. F. & LASEK, A. 1990 Splashing of drops. *Arch. Mech.* **42**, 507.

MEIER, G. E. A., KLÖPPER, A. & GRABITZ, G. 1992 The influence of kinematic waves on jet break down. *Exps. Fluids* **12**, 173.

MIKAMI, T., COX, R. G. & MASON, S. G. 1975 Breakup of extending liquid threads. *Intl. J. Multiphase Flow*, **2**, 113.

NABER, J. D. & FARRELL, P. V. 1993 Hydrodynamics of droplet impingement on a heated surface. *SAE Paper* 930919.

O'BRIEN, S. B. G. M. 1993 On Marangoni drying: nonlinear kinematic waves in a thin film. *J. Fluid Mech.* **254**, 649.

PEREGRINE, D. H. 1981 The fascination of fluid mechanics. *J. Fluid Mech.* **106**, 59.

PEREGRINE, D. H., SHOKER, G. & SYMON, A. 1990 The bifurcation of liquid bridges. *J. Fluid Mech.* **212**, 25.

PROSPERETTI, A. & OĞUZ, H. N. 1993 The impact of drops on liquid surfaces and the underwater noise of rain. *Ann. Rev. Fluid Mech.* **25**, 577.

RAYLEIGH, LORD 1878 On the instability of jets. *Proc. Lond. Math. Soc.* **10**, 4.

REIN, M. 1993 Phenomena of liquid drop impact on solid and liquid surfaces. *Fluid Dyn. Res.* **12**, 61.

RIEDEL, E. 1977 Geräusche aufprallender Wassertropfen. *Acustica* **38**, 89.

SCHLICHTING, H. 1979 *Boundary-Layer Theory*. McGraw-Hill.

SCHNEIDER, J. M. & HENDRICKS, C. D. 1964 Source of uniform-sized liquid droplets. *Rev. Sci. Instrum.* **35**, 1349.

SHARMA, A. & RUCKENSTEIN, E. 1988 Dynamics and lifetimes of thin evaporating liquid films: some non-linear effects. *Phys. Chem. Hydrodyn.* **10**, 675.

STOW, C. D. & HADFIELD, M. G. 1981 An experimental investigation of fluid flow resulting from the impact of a water drop with an unyielding dry surface. *Proc. R. Soc. Lond.* A **373**, 419.

STOW, C. D. & STAINER, R. D. 1977 The physical products of a splashing water drop. *J. Met. Soc. Japan* **55**, 518.

SULTANOV, F. M. & YARIN, A. L. 1990 Percolation model of a disintegration and explosive atomization of liquid medium: drop-size distribution. *J. Appl. Mech. Tech. Phys.* **31**, 48.

TAYLOR, G. I. 1934 The formation of emulsions in definable fields of flow. *Proc. R. Soc. Lond.* A **146**, 501.

TAYLOR, G. I. 1959 The dynamics of thin sheets of fluid II. Waves on fluid sheets. *Proc. R. Soc. Lond.* A **253**, 296.

TOMOTIKA, S. 1936 Breaking up of a drop of viscous liquid immersed in another viscous fluid which is extending at a uniform rate. *Proc. R. Soc. Lond.* A **153**, 302.

WEISS, D. A. 1993 Periodischer Aufprall monodisperser Tropfen gleicher Geschwindigkeit auf feste Oberflächen. *Mitteilungen aus dem Max-Planck-Institut für Strömungsforschung, Göttingen*, Nr. 112.

WHITHAM, G. B. 1974 *Linear and Nonlinear Waves*. Wiley.

WORTHINGTON, A. M. 1876 On the forms assumed by drops of liquids falling vertically on a horizontal plate. *Proc. R. Soc. Lond.* A **25**, 261.

WORTHINGTON, A. M. 1877 A second paper on the forms assumed by drops of liquids falling vertically on a horizontal plate. *Proc. R. Soc. Lond.* A **25**, 498.

WORTHINGTON, A. M. 1908 *A Study of Splashes*. London: Longmans, Green, and Co.

YARIN, A. L. 1993 *Free Liquid Jets and Films: Hydrodynamics and Rheology*. Longman and Wiley & Son.

YARIN, A. L., ORON, A. & ROSENAU, PH. 1993 Capillary instability of thin liquid film on a cylinder. *Phys. Fluids* A **5**, 91.

ZELDOVICH, YA. B., BARENBLATT, G. I., LIBROVICH, V. B. & MAKHVILADZE, G. M. 1985 *Mathematical Theory of Combustion and Explosions*. New York: Consultants Bureau.